Melt pond fraction and spectral sea ice albedo retrieval from MERIS data I: validation against in situ, aerial, and ship cruise data

L. Istomina[1], G. Heygster[1], M. Huntemann[1], P. Schwarz[2], G. Birnbaum[3], R. Scharien[4], C. Polashenski[5], D. Perovich[5], E. Zege[6], A. Malinka[6], A. Prikhach[6] and I. Katsev[6]

[1]{Institute of Environmental Physics, University of Bremen, Bremen, Germany}

[2]{Department of Environmental Meteorology, University of Trier, Trier, Germany}

[3]{Alfred Wegener Institute, Helmholtz Centre for Polar and Marine Research, Bremerhaven, Germany}

[4]{Department of Geography, University of Victoria, Victoria, Canada}

[5]{Cold Regions Research and Engineering Laboratory, Engineer Research and Development Center, Hanover, New Hampshire, USA}

[6]{B.I. Stepanov Institute of Physics, National Academy of Sciences of Belarus, Minsk, Belarus}

Correspondence to: L. Istomina (lora@iup.physik.uni-bremen.de)

Abstract

The presence of melt ponds on the Arctic sea ice strongly affects the energy balance of the Arctic Ocean in summer. It affects albedo as well as transmittance through the sea ice, which has consequences for the heat balance and mass balance of sea ice. An algorithm to retrieve melt pond fraction and sea ice albedo from MEdium Resolution Imaging Spectrometer (MERIS) data is validated against aerial, ship borne and in situ campaign data. The results show the best correlation for landfast and multiyear ice of high ice concentrations. For broadband albedo R^2 is equal to 0.85, with the RMS being equal to 0.068, for the melt pond

1

fraction: R^2 is equal to 0.36 with the RMS being equal to 0.065. The correlation for lower ice concentrations, subpixel ice floes, blue ice and wet ice is lower due to ice drift and challenging for the retrieval surface conditions. Combining all aerial observations gives a mean albedo RMS of 0.089 and a mean melt pond fraction RMS of 0.22. The in situ melt pond fraction correlation is $R^2=0.52$ with an RMS=0.14. Ship cruise data might be affected by documentation of varying accuracy within the Antarctic Sea Ice Processes and Climate (ASPeCt) protocol, which may contribute to the discrepancy between the satellite value and the observed value: mean $R^2=0.044$, mean RMS=0.16. An additional dynamic spatial cloud filter for MERIS over snow and ice has been developed to assist with the validation on swath data.

1 Introduction

Melt ponds on the Arctic sea ice affect the albedo, mass balance and heat balance of the ice (e.g. Perovich et al., 2009) by translating the increase of air temperature into drastic and rapid surface type changes. They introduce a positive feedback within the sea ice albedo feedback loop (Curry et al., 1995) thus facilitating further ice melt. In the context of changing Arctic climate (Shindell and Faluvegi, 2009), knowledge of melt pond fraction (MPF), its spatial distribution and the length of the melt season is required to reflect and predict the role of the sea ice cover in the radiative balance of the region. Schröder et al. (2014) show the potential of predicting the minimum sea ice extent in autumn by the spring MPF. In addition to applications in climate studies, e.g. global circulation modeling, knowledge of the MPF can be helpful for navigation purposes. Findings from numerous in situ campaigns (Barber and Yackel, 1999; Hanesiak et al., 2001; Yackel et al., 2000) provide data of excellent quality and detail, but unfortunately lack in coverage. To fill in this gap, a remote sensing approach needs to be employed.

The present work is dedicated to validation of a MPF and sea ice albedo retrieval algorithm, the Melt Pond Detector (MPD), described by Zege et al., (2015). The algorithm differs from existing satellite remote sensing algorithms, e.g. Rösel et al., (2012) or Tschudi et al., (2008), by 1) utilizing a physical model of sea ice and melt ponds with no a priori surface spectral relectances, and 2) providing daily averaged MPF instead of weekly averaged MPF, which is beneficial in case of rapid melt evolution. Field observations (Figure 1) show faster melt

evolution on first year ice (FYI) as compared to multiyear ice (MYI). Due to the fact that MPF depends not only on air temperature and available melt water volume but also on the ice topography (Eicken et al., 2004; Polashenski et al., 2012), the melt evolution is different for FYI and MYI. Melt onset proceeds rapidly to the MPF maximum on FYI with rapid pond drainage and moderate MPFs afterwards. On multiyear ice, the evolution of melt up to the melt maximum takes longer. The peak MPF value is lower and the MPF decrease is slower than that on FYI (Figure 1). A detailed description of melt stages and melt water distribution mechanisms can be found in Polashenski et al., (2012). These details of melt evolution are responsible for the spatial variability of MPF and sea ice albedo. The temporal variability of MPF is driven by air mass transport and changing air temperature. This introduces complications in the MPF modeling and creates the need for an MPF and sea ice albedo dataset of possibly high temporal and spatial resolution, which can be retrieved from satellite data.

The manuscript is structured as follows: in Section 2 the MPD algorithm, its input and output data are described. Section 3 is dedicated to validation of the cloud screening (Sect. 3.1), albedo (Sect. 3.2) and MPF (Sect. 3.3) products. The additional cloud screening developed for the purpose of quality validation is presented in Section 3.3.2. The conclusions are given in Section 4.

2   Data used

The data used for the present study are the pond fraction and broadband sea ice albedo swath data products retrieved from MERIS swath Level 1b data over the ice covered Arctic Ocean using the MPD retrieval. The present chapter presents a short summary of the MPD retrieval. The full description of the algorithm can be found in Zege et al., (2015).

The MPD is an algorithm for retrieving characteristics (albedo and melt ponds fraction) of summer melting ice in the Arctic from data of satellite spectral instruments. In contrast to previously developed algorithms (Rösel et. al, 2012; Tschudi et al., 2008) MPD does not use a priori values of the spectral albedo of constituents of the melting ice (melt ponds, drained surface, etc.).

The retrieval algorithm is based on the observations of optical properties of constituents of sea-ice (Perovich, 1996). A sea ice pixel is considered as consisting of two components: white

3

ice and melt ponds. The reflection properties of surface are described by the spectral bi-directional reflectance distribution function (BRDF) $R(\theta, \theta_0, \varphi, \lambda)$, where θ and θ_0 are the zenith angles of the observation and illumination directions, respectively, and φ is the azimuth angle between them, λ is the wavelength.

The white ice is considered as an optically thick weakly absorbing layer. The BRDF of this sub-pixel $R_{ice}(\theta, \theta_0, \varphi, \lambda)$ is determined by its optical depth τ_{wi}, the mean effective grain size a_{eff}, and the absorption coefficient α_{yp} of yellow pigments, which could arise due to sediments suspended in the seawater. The spectral dependencies of optical characteristics of a layer are determined by the spectrum of the complex refractive index of ice by (Warren and Brandt, 2008) and spectral absorption of yellow pigments by (Bricaud et al., 1981). The used analytical approximation for $R_{ice}(\theta, \theta_0, \varphi, \lambda)$ has been developed on the base of the asymptotic solution of the radiative transfer theory (Zege et al., 1991).

The BRDF of a melt pond $R_{pond}(\theta, \theta_0, \varphi, \lambda)$ is determined by the melt water optical depth τ_p and by the spectral albedo of its bottom. The pond bottom is an ice layer, which in turn is characterized by the transport scattering coefficient σ_{ice} and the optical depth τ_{ice}. Thus, the BRDF of the melt pond is calculated as reflection of the water layer with a semi-translucent bottom.

It is supposed that the pixel surface consists of white ice (highly reflective) and melt ponds with area fraction S. The BRDF of the whole pixel is a linear combination:

$$R(\theta, \theta_0, \varphi, \lambda) = (1 - S)R_{ice}(\theta, \theta_0, \varphi, \lambda) + SR_{pond}(\theta, \theta_0, \varphi, \lambda) \qquad (1)$$

The body of the retrieval algorithm comprises of the following steps.

1. The input to the algorithm is the MERIS level 1B data, including the radiance coefficients R_i at channels i=1, 2, 3, 4, 8, 10, 12, 13, 14 (correspond to the central wavelengths of 412.5, 442.5, 490, 510, 681.25, 753.75, 778.75, 865 and 885nm), and the solar and observation angles (zenith and azimuth). Also the relevant information on atmosphere and surface state can be entered from an input file.

2. The data is sent to the three independent blocks:

4

a. The atmospheric correction preprocessing block. The atmosphere reflectance r_i and transmittance t_i are calculated for the used set of wavelengths (i is the channel number). Atmospheric correction is performed with regard to the surface BRDF.

b. Separation of the sea-ice pixels. In this procedure the ice pixels are separated from the cloud, land and open water pixels, using a brightness criterion on the channels R_2, R_3, and R_4, spectral neutrality criterion on the ratio of the channels R_1 and R_2, MERIS differential snow index (Schlundt et al., 2011) and the threshold on the ratio of the MERIS oxygen-A band (R_{11} and R_{10}). The first two criteria separate white surfaces, which can be snow, ice, or cloud. The MERIS differential snow index and oxygen-A band threshold discard cloudy pixels over snow.

c. Setting the bounds for ice and pond parameters. These border values serve to stabilize the algorithm and are set to correspond to values observed in nature (obtained by analyzing the field data from the Polarstern cruise (Istomina et al., 2013) and from the CRREL field observations (Polashenski et al., 2012)).

3. The main part of the algorithm is an iterative procedure to retrieve ice and pond parameters and the pond fraction S. The procedure is based on the Newton-Raphson method (Press et al., 1987) that provides the search of the minimum of the functional $\sum_i (R_i^{meas} - R_i^{calc})^2$ in the space of ice and ponds characteristics and fraction S.

4. The resulting characteristics and the value of S are used to calculate the spectral albedo of the pixel.

5. Output is the melt pond area fraction, the spectral albedo, and the estimation of the retrieval error in the pixel. The spectral albedo is retrieved at six wavelengths specified by the user. For the validation studies presented in this paper, the broadband sea ice albedo has been calculated as an average of the six spectral albedo values at 400-900nm in steps of 100nm.

A satellite scene is processed pixel by pixel, producing an hdf5-formatted map of output values.

5

The MPD algorithm has been preliminarily verified numerically, using a synthetic dataset of top of atmosphere radiances from melting Arctic ice as the input of a satellite spectral instrument. This dataset was computed with software developed based on the radiative transfer code RAY (Tynes et al., 2001; Kokhanovsky et al., 2010) for calculating signals reflected by the melting sea ice-atmosphere system. Thus the radiances in the MERIS spectral channels were simulated for a set of ice pixels for a few typical situations, including 'standard' white ice, bright ice (snow covered), dark and light blue melt ponds. The numerical experiment showed that the melt pond fraction can be retrieved with high accuracy (error less than 1%) for the most common case of 'standard' white ice and light blue (young) melt pond. The retrieval error increases with deviation from the 'standard' case, e.g. the retrieved pond fraction can be underestimated more than twice for the case of bright (snow covered) ice and dark (mature) melt pond. However, this situation is rare, because in the case of an open (exposed) mature pond snowfall only affects the surrounding ice surface for a short time due to melt temperature. The case of lid covered melt pond is a separate topic, which is discussed in detail in Sect. 3.3.3. Submerged sea ice or water saturated ice surface are optically identical to melt ponds and are retrieved as those. At the same time the MPD algorithm provides accurate retrievals of the spectral albedo in all considered cases, even in the situations when the error of the pond fraction retrieval is high. The spectral albedo is retrieved much better with the MPD algorithm than with the conventional algorithms using the Lambert approximation for surface reflection, which underestimates the albedo at about 0.05 all over the spectral range, whereas the error of the MPD retrieval in the worst case ('bright ice – dark pond') is 0.01 and lower in all other considered cases.

3 Validation

The datasets used for the validation of the MPD algorithm are shown in Table 1.

These validation datasets contain a wide range of pond fractions and were obtained over landfast ice, FYI and MYI of various ice concentrations. Therefore the performance of the satellite retrieval can be thoroughly tested for a variety of conditions and conclusions on the more or less suitable conditions for the application of the MPD retrieval can be drawn. Such conclusions are especially important as the MPD retrieval was initially designed for a limited set of ice and pond parameters, namely for the conditions of the melt evolution with open

6

melt ponds surrounded by dry white ice within the pack ice. A sensitivity study based on modeled input data shows the algorithm's better performance for bright melt ponds as opposed to dark melt ponds (Zege et al., 2015). Therefore, it is expected that the MPD algorithm shows the best performance over MYI of high ice concentrations. The performance over lower ice concentrations, in case of subpixel ice floes, saturated wet dark ice or thin ponded ice is compromised due to the limitations of the retrieval (Zege et al., 2015). We, however, perform the comparison to the in situ data for all available conditions anyway in order to evaluate the performance of the algorithm at the global scale.

Unfortunately, MERIS only features VIS and NIR channels, whereas for effective cloud screening over snow, IR and TIR channels would be more suitable. Therefore MERIS is not the best instrument for cloud screening over snow and ice, and there remains a risk of cloud contamination in the swath data and final gridded product. To avoid this, an additional cloud screening (Sect. 3.3.2) was implemented which proved to give a much better result on swath data. For the gridded product, a restriction on the amount of valid data pixels to form one grid cell was applied to screen out cloud edges. These issues will be addressed below.

The summary of dataset locations is shown in Figure 2. Among the above mentioned datasets, the airborne measurements and transect estimates are more accurate than visual estimations; in case of ship cruise bridge observations or visual estimations of melt ponds fraction in the field, the measurement accuracy is hard to evaluate.

3.1 Validation of the cloud screening

3.2 In order to test the performance of the cloud screening presented in Zege et al., (2015), we have employed data from the AATSR sensor aboard the same satellite platform. The advantage of this sensor is that it has suitable IR channels for cloud screening over snow and ready procedures to perform this task. For this study, a cloud screening method for AATSR developed by Istomina et al., (2010) is used. For that, the swath data of both MERIS and AATSR was collocated and cut down to only AATSR swath. Then, the two cloud masks (the reference mask by AATSR and test mask by MERIS) have been compared as follows: for each swath, an

average pond fraction in cloud free areas as seen by AATSR (Figure 3, blue curve) and by MERIS (Figure 3, red curve) has been derived. This has been done for the period from May 1, 2009 to September 30, 2009. The resulting Figure 3 shows the effect of clouds on the MERIS MPD swath data: before the melt season, clouds have lower albedo than the bright surface and may be seen as melt ponds by the MPD retrieval. In the case of developed melt, the situation is the opposite: the melting surface is darker than clouds, and unscreened clouds are taken as lower pond fraction by the retrieval. Overall, the unscreened clouds in the MPD product result in smoothing out of the pond fraction toward the mean value of about 0.15. However, the temporal dynamics is preserved even in swath data. Partly the problem of unscreened clouds can be solved at the stage of gridding swath data into daily or weekly averages, by constraining the amount of valid pixels that form a valid grid cell so that cloudy areas which are only partly unscreened in the swath data are still not included in the gridded data (see Sect. 2 in the companion paper Istomina et al., 2015). It is important to note the positive MPF bias even in the data cloud screened with the reference AATSR cloud mask (blue curve in Figure 3) both in May and in September 2009 where no melt ponds should be present. One of the reasons for the bias in September might be the specifics of the MPD retrieval which detects also frozen ponds as MPF (see Sect. 3.3.3 for details). Another reason might be the actual accuracy issues of the MPD retrieval for dark ponds (see Zege et al., (2015) for details). Given the geographical coverage of the study region (Arctic Ocean to the north of 65°N), the positive MPF bias in May can appear due to water saturated sea ice (after the onset of positive air temperature but before the actual widespread melt). Validation of the albedo product

3.2.1 In situ validation

8

Validation of the sea ice albedo satellite retrieval is a non-trivial task due to high spatial variability. In summer this variability is even more pronounced as each given duration and intensity of melt or refreeze creates an optically unique surface type (various grain sizes of sea ice and snow, drained, forming, overfrozen melt ponds, deep or shallow ponds on MYI or FYI, intermediate slushy areas, etc). For a satellite pixel size of 1.2 km x 1.2 km the surface types and their fractions from field observations are in the best case only known for a 100-200 m long transect. In order to obtain the in situ sea ice albedo, a linear mix of all surface fractions is constructed. The availability of such comprehensive field measurements is very limited, and for those available, the question of how representative the chosen transect is for the whole area is anyway present. In this study, we use a transect data taken in the Canadian Arctic in June and July 2006 as part of the joint Finnish Institute of Marine Research and University of Calgary Cryosphere Climate Research Group polar ice POL-ICE research project (Geldsetzer et al., 2006), where the uniform pond distribution was confirmed using helicopter images (not shown here).

During POL-ICE 2006 the spatio-temporal evolution of surface features and their spectral reflectance properties were monitored by collecting a series of transect measurements on landfast FYI (FI) also in the vicinity of Resolute Bay, Nunavut between June 26, 2006 and July 11, 2006. For each transect, a 200m transect line was established perpendicular to the predominant major-axis pond direction to maximize the frequency of changes between ponds and snow/bare ice patches. For the relatively uniformly distributed network of ponds and snow/bare ice patches characteristics of smooth FYI, this orientation yields a representative areal fraction of cover types (Grenfell and Perovich, 2004). A total of 12 transects were collected with surface cover types classified as: melt pond, snow/bare ice, or mixed at 0.5 m intervals. The mixed cover type was introduced to classify the slushy mixture of water saturated ice that could be neither classed as discrete pond or snow/bare ice. The data is shown in Table 2.

For 8 of POL-ICE 2006 transects when lighting conditions were suitable, cosine-corrected downwelling and upwelling radiance (0.35 m height) measurements were made at 2m intervals using a TriOS RAMSES spectrometer (320-950nm). Spectral data were processed using the calibration files and software bundled with the RAMSES spectrometer, with radiation measurements integrated across the bandwidth of the instrument to create integrated

9

albedo measurements from each sample. Each albedo measurement was matched to a surface class, and average broadband albedo statistics by class and for each transect were derived. For these locations, the MPD retrieval has been performed and the broadband albedo average within 5km around the location has been produced. Satellite overflights closest in time to the field measurements were taken. The result is shown in Table 3, the comparison itself in the last column „Results". The NaNs in the retrieved data are gaps due to cloud cover. Only four cases were cloud free. Overall, slight overestimation of the satellite albedo is visible. The discrepancies between the field and satellite albedo can be explained by difference in the spatial resolution of the two datasets and varying melt pond distribution within the studied area.

3.2.2 Aerial validation

The validation has been performed for selected cloud free satellite swaths at the reduced resolution of the retrieval (MERIS data, reduced resolution, 1.2 km x 1.2 km).

The aircraft campaign MELTEX („Impact of melt ponds on energy and momentum fluxes between atmosphere and sea ice") was conducted by the Alfred Wegener Institute for Polar and Marine Research (AWI) in May and June 2008 over the southern Beaufort Sea (Birnbaum et al., 2009).

The campaign aimed at improving the quantitative understanding of the impact of melt ponds on radiation, heat, and momentum fluxes over Arctic sea ice. For determining broadband surface albedo, the BASLER BT-67 type aircraft POLAR 5 was equipped with two Eppley pyranometers of type PSP measuring the broadband hemispheric down- and upwelling shortwave radiation. The radiation sensors were mounted on the aircraft in a fixed position. For clear-sky conditions, data of the upward facing pyranometer, which receives direct solar radiation, were corrected for the misalignment of the instrument (based on a method described by Bannehr & Schwiesow, (1993)) and the roll and pitch angles of the aircraft to derive downwelling hemispheric radiation flux densities for horizontal exposition of the sensor (see Lampert et al., 2012).

Weather conditions in May 2008 were characterized by warming events interrupted by cold-air advection from the inner parts of the Arctic towards the coast of the southern Beaufort

Sea. A warming event on May 23 and May 24, 2008, caused the onset of melt pond formation on ice in a large band along the coast from the Amundsen Gulf to Alaska. On May 26, 2008, numerous melt ponds in a very early stage of development were overflown. However, from May 27 to June 1, 2008, a new period with prevailing cold-air flow caused a refreezing of most melt ponds, which were still very shallow at that time. During the last week of the measurements, a tongue of very warm air was shifted from Alaska to the Beaufort Sea. It reached its largest extension over the ocean on June 4 and June 5, 2008, which again strongly forced the development of melt ponds.

The available validation data consist of 5 flight tracks for 5 days on May 26, and June 3, June 4, June 6 and June 7, 2008. Only the cloud free data is selected. The measurements were performed at different altitudes, as low as 50m and reaching 400m, with correspondingly different numbers of measurement points for each satellite pixel. The collocation of such an uneven dataset with the satellite data has been performed by calculating an orthodromic distance of every pixel within a satellite swath to a given aerial measurement point, and collecting those aerial points lying at the minimum distance to the centre of a given satellite pixel. This ensures that aerial measurements performed at any height are collocated to the corresponding satellite pixel correctly. The number of data points per flight is in the order of tens to hundreds of thousands with up to 500 points per satellite pixel.

The validation effort has been done on swath satellite data. The quality of retrieval conditions for the MPD algorithm differs for each overflight depending on weather conditions, ice concentration and ice type. In addition, time difference between the satellite overflight and aerial measurements affect the comparison (Table 4) due to ice drift.

An example of such different conditions is shown in Figure 4, where the flight tracks over FI and over separate ice floes are shown.

The time difference between the aerial measurement and satellite overflight varies for the presented cases, which adds to the validation data uncertainty for cases with lower ice concentrations due to drifting separate floes. Where possible in case of drift, the time difference was limited to 1.5 hours around the satellite overflight. Two exceptions with time difference 2^h-3^h are marked in Table 4. Figure 5 shows the altitude and the correlation of the measured and retrieved broadband albedo for the only flight over FI on June 06, 2008. The

11

1 rest of the flights were flown over separate floes. As no screening of albedo data was possible,

2 it was decided to limit the time difference to 1.5 hour around the satellite overflight for the

3 asymmetrically distributed flights. Some points of low measured albedo but high retrieved

4 albedo feature time difference up to 2h and are most probably connected to the drift of

5 separate ice floes. These are flights on June 04, 2008, May 26, 2008, June 03, 2008 and June

6 07, 2008. They are shown in Figure 6, Figure 7 and Figure 8. Due to ice drift, the aerial

7 measurements are displaced relative to the satellite snapshot which causes different areas to

8 be compared to each other. The resolution differences of the two sensors may increase this

9 difference even more. Therefore, slight over or underestimation due to the ice concentration

10 difference of aerial and satellite measurements is visible. As the numerical experiment shows

11 that accuracy of the albedo retrieval in all cases is high (Zege et al., 2015), and the case of no

12 drift shows high correlation of retrieved and measured albedo (fast ice (FI) case shown in

13 Figure 5), we conclude that the discrepancy is due to the specifics of data used for validation

14 and not a weak point of the MPD retrieval. To conclude, the best correlation for albedo

15 retrieval is observed for the landfast ice, which are the conditions of the best algorithm

16 performance with R^2=0.85, RMS=0.068. Due to the lack of field data the validation has not

17 been performed over MYI, however, the MPD has been designed for MYI, namely sea ice of

18 high concentration with light melt ponds. FI is a deviation from this case at least in the melt

19 pond type, and potentially in the surface albedo, but as MPD performed well even in this case,

20 we expect it's performance to be at least as good over MYI of high ice concentrations.

21 Correlation for lower ice concentrations, subpixel ice floes, blue ice and wet ice is lower due

22 to complicated surface conditions and ice drift. Combining all aerial observations gives a

23 mean albedo RMS of 0.089.

24 **3.3   Validation of the melt pond product**

25 **3.3.1   Aerial validation**

26 For the validation of the melt pond product, the aerial photos from the same airborne

27 campaign MELTEX 2008 have been used. Although the flight tracks are the same, the criteria

28 for data selection are different for albedo and melt pond measurements. This is why the

29 validation data for melt pond and albedo data not to overlap entirely for the same flight. The

12

1   number of points per flight is in the order of hundreds with about 5 images per satellite pixel

2   (example photograph is shown in Figure 9). Additionally, one more flight over MYI near the

3   coast of North Greenland during the aerial campaign NOGRAM-2 2011 has been used.

4   For the evaluation of the aerial photographs a supervised classification method (maximum

5   likelihood) was applied. For every pixel x, the probability D of belonging to every class c is

6   calculated. The pixels get assigned to the class with the highest probability (Jensen, 2008). If

7   the training data is normally distributed, the maximum likelihood is expressed as follows

8   (Gonzalez and Woods, 2002):

9   $$D = \ln(a_c) - [0.5\ln(|Cov_c|)] - [0.5(X - M_c)^T (Cov_c^{-1})(X - M_c)]. \qquad (2)$$

10 where D is the quantities weighted distance (likelihood), c is a particular class, X is the

11 measurement vector of the candidate pixel, M_c is the mean vector of the sample of class c, a_c

12 is the a priori probability of class c (set to equal values for all classes), Cov_c is the covariance

13 matrix of the pixels in the sample of class c, T is the transposition function.

14 More than 10,000 aerial photographs were recorded during the MELTEX campaign during

15 the different flight tracks. As the quality of the data was not uniform, only images which meet

16 the following requirements were chosen: images taken during horizontal flight tracks (to

17 minimize the geometric distortions) and clear sky flight tracks (to prevent a wrong

18 classification because of fog, clouds and shadows of the clouds). The camera was operated

19 with a non-constant exposure, so that the sea ice in images with a large fraction of open water

20 was overexposed and useless for further evaluation. To simplify the automated classification,

21 images of each day were separated into different flight tracks with similar exposure, ice

22 conditions and same flight level. Nevertheless almost 3000 images were classified and

23 evaluated for the MELTEX campaign. Two suitable flight tracks of the NOGRAM-2

24 campaign that contain about 1000 images were chosen to complement the quantification of

25 the melt stages. Depending on the flight level, each image covered an area between 0.2 km^2

26 and 3 km^2.

27 Overall the validation data used features four types of sea ice: thin and thick FYI as well as FI

28 for the MELTEX images, and MYI for NOGRAM-2. Most of the investigation area of the

29 MELTEX campaign was covered by thin FYI or FI. Only on June 07, 2008, the most

30 northerly part of the flight track contained a notable amount of thick FYI. This part showed a

13

1   different behavior during the melting process and contained different surface classes than the

2   thin FYI or FI.

3   Most flight tracks of the campaign were subdivided in several subflight tracks. For every

4   subflight track a representative image was chosen, which contained all classes. In cases where

5   there were no representative images with all classes for a given subflight track, two or more

6   images were merged for the determination of the training data. The threshold for the

7   maximum likelihood method was set to 0.95. This means that the probability of belonging to

8   a defined class must be 0.95 or higher. Otherwise the pixels were not classified. Within the

9   presented study, the amount of unclassified pixels per image is uniformly about 1-2%.

10 The sea ice conditions varied greatly for each of the studied flights, with the cases ranging

11 from land fast ice of 100% ice concentration, separate drifting ice floes to brash ice with

12 subpixel ice floes (example in Figure 10). The cases with no separate ice floes and no ice drift

13 are shown in Figure 11 (FI) and Figure 12 (left panel, MYI) with quite good correspondence

14 of the retrieved and measured pond fractions. Right panel in Figure 12, on the other hand,

15 shows higher retrieved MPF than measured from the aircraft. The reason for this discrepancy

16 is twofold: relatively large time difference and the challenging surface conditions. The surface

17 state at the time was as follows: the reported cold air intrusion in the area on June 01, 2008

18 prevented the forming melt ponds from evolving further (an overview on surface conditions

19 in the area can be found in Scharien et al., (2012)), and the large floes were covered with

20 frozen ponds at the beginning of their evolution. Frozen shallow ponds at the beginning of their

21 evolution were classified as sea ice from the aerial images, but retrieved as melt ponds from the

22 satellite. For the applications connected to the radiation budget studies (e.g., GCM), a

23 generalization where darker types of sea ice and melt ponds are put into one class is appropriate

24 due to similar radiative characteristics of the two.

25 Figure 13 shows the flight on June 07, 2008, which features larger ice floes than the flights

26 shown in Figure 14. The MPF output of the MPD algorithm is not affected by the subpixel

27 fraction of open water because the almost constant spectrum of open water only affects the

28 amplitude and not the spectral shape of the mixture of surfaces (sea ice, ponds and open

29 water) within the pixel; however, the spectral signature of melt ponds is harder to resolve in

30 case of lower ice concentrations. Subpixel ice floes, brash ice, blue ice are not appropriate

14

1 conditions for the MPD algorithm application, hence the overestimated pond fraction for both

2 flights in Figure 14. Overall, the best correlation can be seen for the cases of landfast and

3 multiyear ice of high ice concentrations R^2=0.36, RMS=0.065. Combining all aerial

4 observations gives mean melt pond fraction RMS equal to 0.22.

5 ### 3.3.2 Cloud screening for in situ and ship cruise validation

6 As the aerial validation has been performed on cloud free data, the problem of cloud clearing

7 did not arise. For in situ and ship cruise data, cloud contamination may increase the

8 uncertainty of the satellite retrieved values and in these cases this problem has to be addressed

9 additionally. With the gridded product, the unscreened cloud edges and partly screened out

10 clouds are cut out with the criterion for minimum valid data pixels allowed within one grid

11 cell. For the swath data, such criterion is not applied and the existing cloud filtering proved to

12 be not sufficient for a quality validation. Therefore, an additional spatial dynamic filter was

13 introduced for ship cruise and in situ data. An example is shown in Figure 15.

14 The dynamic spatial filter consists of dividing the swath into boxes of 10x10 pixels with all

15 the surface and cloud screening criteria applied except the oxygen A filter (Eq. 5 in Zege et

16 al., (2015)); due to MERIS bands specifics, all these filters are imperfect and are subject to

17 misclassifying certain types of clouds (e.g. thin clouds and ice clouds) as ice and snow. Then,

18 within a given box, the oxygen A filter is applied. If this additional oxygen A filter screened

19 out some additional pixels, then the box is potentially cloudy and the imperfect cloud filters

20 surely left some unscreened clouds. Such a box is discarded completely. If the additional

21 oxygen A filter (which is more sensitive to high and thick low clouds than the other applied

22 cloud filters, so in the case of clouds it would screen out more pixels than the other filters) did

23 not screen out any additional pixels, the scene is either uniformly filled with just clouds to

24 which none of the filter are sensitive (improbable) or it is a cloud free scene. The boxes where

25 this happens are kept and used for validation.

26 This method proved to be successful for the case studies on single swaths which do not

27 undergo gridding with a threshold on the minimum allowed amount of cloud free pixels

28 which helps to screen out cloud edges or partly screened clouds. For our MERIS gridded

29 products, the gridding procedure tends to introduce a similar cloud screening effect as the

15

1 above mentioned filter. High thin clouds, however, may still be present within both swath

2 data and gridded products. The consequences are discussed in the Section 3.1.

3.3.3 Ship cruise validation

4 The visual estimations of various sea ice parameters, including MPF during the ship cruises

5 differ in accuracy from aerial measurements, transect measurements, or visual estimations

6 during in situ campaigns which are dedicated to such measurements. As opposed to the in situ

7 campaign, hourly bridge observations are performed by many observers with different

8 estimation experience and skill, which introduces additional noise to the observed value. The

9 two studied cruises – The Healy-Oden Transarctic Expedition (HOTRAX), 19 August – 27

10 September 2005 (Perovich et al., 2009), and RV Polarstern cruise ARK-XXVI-3

11 (TransArc2011), 04 August 2011 – 6 October 2011 (Nicolaus et al., 2012), - both travelled

12 across the Arctic Ocean at the end of melt season, August-September. The occurrence of

13 frozen over, snow covered or entirely melted through melt ponds was therefore high. The ice

14 observations during both cruises have been performed within the Antarctic Sea Ice Processes

15 and Climate (ASPeCt) protocol. The specifics of ASPeCt ice watch protocol leads to lack of

16 fields for detailed description of the state of melt ponds. During TransArc2011 such details

17 were sometimes (but not always) mentioned in the field for comments, and for HOTRAX

18 cruise such information was not available at all. Where available these details are helpful for

19 the validation of the MPD algorithm. Spectral reflectance of frozen and snow covered ponds

20 can be represented as a linear mixture of dark pond and sea ice within the MERIS spectral

21 range, and melted through ponds have the spectral behaviour of open water. Both surface

22 types are no longer melt ponds in the original sense of the word and have to be excluded from

23 the retrieved MPF for energy budget or climate modelling applications. As the MPD

24 algorithm utilizes the difference in spectral behaviour of melt ponds, open water and sea ice,

25 it will retrieve the true fraction of open melt ponds with sea ice underneath the meltwater. In

26 case of melted through or frozen over ponds documented as melt ponds in the ship based

27 observations, a discrepancy between the ship cruise data and the MPF retrieval will occur.

28 This is illustrated for the case of the frozen snow covered melt ponds in Figure 16. The MPD

29 will continue to retrieve some MPF also in case of frozen ponds as long as their albedo is

30 lower than the albedo of surrounding sea ice. Typically a few centimeters of snow is already

16

enough to even out this albedo difference, but horizontal snow redistribution due to winds can prolong the period of apparent pond presence according to the MPD retrieval. This explains the positive MPF bias in September (after the melt season) in Figure 3.

Within this work, we apply the MPD algorithm without limitations other than cloud screening (original as described by Zege et al., (2015), and dynamic spatial filter described in Sect. 3.3.2) to illustrate the effect of the above mentioned underestimation. In cases not dedicated to the study of the algorithm accuracy, it is recommended to use the MPD MPF product in combination with the reanalysis air surface temperature to apply the algorithm only when the melt ponds are not frozen over. Otherwise the (supposedly low) MPF value is ambiguous and could indicate both low MPF of open ponds or high MPF of frozen ponds.

Both cruises TransArc2011 (Figure 17) and HOTRAX 2005 (Figure 18) had only several days of cloud free collocations. The available swath data and the hourly ship observations have been compared point by point without temporal averaging. The only averaging was the 15km spatially of the satellite data around the ship location. For both cruises, information on ice concentration was available from bridge observations and the ship MP values have been corrected for ice concentration to give the pond fraction relative to the visible area and not to the area of sea ice. For the TransArc2011 cruise, information on MYI and FYI ice concentration was available with corresponding MPFs. The total MPF was calculated using the linear mix of these values. However, the resulting cloud free collocations feature mostly FYI cases. For the HOTRAX 2005, such information was not available and only total ice concentrations were used. The correlation between the satellite value and observed value: mean R^2=0.044, mean RMS=0.16. The low correlation might be caused by the documentation of varying accuracy within the ASPeCt protocol.

3.3.4 In situ validation

The in situ validation has been performed on the swath data using the three available datasets: transect measurements on the FI just north of Barrow, AK, approximately 1km offshore from Niksiuraq in the Chukchi sea, near 71°22´ N, 156°33´ W throughout June 2009 (Polashenski et al., 2012), 100m transect and visual estimations on the 3x3 km area of landfast FYI approximately 80 km northwest of Resolute Bay, Nunavut, 75°14´ N, 97°09´ W, between June 18 and July 10, 2002 as part of the Collaborative Interdisciplinary Crysophere

17

1 Experiment (C-ICE) 2002 project (Scharien and Yackel, 2005), and 200m transect fractions

2 on landfast FYI also in the vicinity of Resolute Bay, Nunavut, 74°44′ N, 95°06′ W, between

3 June 26 and July 11, 2006 (Sect. 3.2.1).

4 During C-ICE 2002 visual estimates of MPF fraction were made on a homogeneous and

5 relatively smooth zone of FI in the Canadian Arctic Archipelago approximately 80 km

6 northwest of Resolute Bay, Nunavut between June 18, 2002 and July 08, 2002 (Scharien and

7 Yackel, 2005). Visual estimates were supported by occasional 100 m transect measurements

8 taken at 0.5 m intervals to characterize surface feature types (melt pond or ice) and pond

9 depths, as well as timelapse photos taken from a tower based camera mounted at 6 m height.

10 From these data a nominal 0.1 MPF estimation error was ascribed to the visual estimates. For

11 days where transect measurements were available, the daily average of W-E and N-S transects

12 was used instead of visual estimates.

13 For the remaining two datasets, the transect measurements of MPFs were used as provided.

14 The datasets feature uniform FI and at times of extremely high pond fractions and the

15 following drainage events. As the campaigns were performed on the FI, no correction for the

16 ice concentration was needed. As in case of ship cruises, the average MPF 15km around each

17 in situ point was taken. The same cloud filtering has been applied (original as described by

18 Zege et al., (2015), and dynamic spatial filter described in Sect. 3.3.2). The total amount of

19 cloud free collocated points is N=47, total RMS = 14%, total R^2=0.52. The correlation plot for

20 the two datasets is shown in Figure 18.

21 **4   Conclusions**

22 Melt ponds on sea ice affect the radiative properties of the ice cover and its heat and mass

23 balance. In order to assess the change of the energy budget in the region (e.g. with GCM),

24 among other sea ice and melt pond properties, the sea ice reflective properties and the amount

25 of melt ponds on sea ice have to be known. This work has validated a retrieval of MPF and

26 broadband sea ice albedo from MERIS data (Zege et al., 2015) against aerial, in situ and ship-

27 based observations.

28 The cloud screening presented in Zege et al., (2015) has been compared to the AATSR cloud

29 screening presented in Istomina et al., (2010) for swath data of both sensors collocated to

18

AATSR swath, for the whole summer 2009. The comparison (Figure 3) shows that unscreened clouds are seen as melt ponds before melt onset and as less melt ponds during melt evolution; the effect of unscreened clouds is not constant and depends on the true surface pond fraction. Unscreened clouds tend to smooth out the melt pond fraction values towards a mean value of about 0.15. As can be seen from the figure, this smoothing effect is most prominent in the beginning of the season and during the melt maximum, and is the smallest in June.

The albedo data from from spaceborne and airborne observations have been compared and showed high correlation when there is no ice drift (Figure 5, Figure 7). Same comparison for MPF highly depends on the ice conditions and melt stage: for FI and MYI in the beginning of melt the correlation is high (Figure 11, Figure 12, Figure 19), for separate FYI floes the correlation is worse maybe due to ice drift (Figure 13, Figure 14). The comparison of ship cruise data to satellite retrieved MPF for FYI and MYI at the end of the melt season shows strong underestimation of satellite retrieval. This might be connected to frozen over ponds undocumented in the ASPeCt observations (Figure 17, Figure 18). At the same time, comparison to ship observations show that the MPD retrieval shows ambiguity of the retrieved MPF: low retrieved MPF could indicate low MPF of open ponds or high MPF of frozen ponds. It is planned to resolve this ambiguity in the future versions of the algorithm by introducing a decision tree based on the air temperature as a measure of surface energy balance to determine whether ponds are frozen over or not.

The presented melt pond fraction and sea ice albedo retrieval can be applied to other radiometers with sufficient amount of channels in the VIS and NIR regions of spectrum, e.g. VIIRS onboard Suomi NPP and OLCI onboard the Sentinel-3 ESA mission (planned launch late 2015). Thus the continuity of the MPF and sea ice albedo dataset can be achieved, which is important for the dataset use as input to GCM and for studies of MPF and albedo dynamics in the context of global change and Arctic amplification.

The case studies, time sequence analysis and trends of MPF and sea ice albedo are presented in the companion paper (Istomina et al., 2015).

Acknowledgements

19

11 **References**

12 Bannehr, L. and Schwiesow, R.: A Technique to Account for the Misalignment of
13 Pyranometers Installed on Aircraft, J. Atmos. Ocean. Technol., 10(5), 774–777,
14 doi:10.1175/1520-0426(1993)010<0774:ATTAFT>2.0.CO;2, 1993.

15 Barber, D. G. and Yackel, J.: The physical, radiative and microwave scattering characteristics
16 of melt ponds on Arctic landfast sea ice, Int. J. Remote Sens., 20(10), 2069–2090, 1999.

17 Birnbaum, G., Dierking, W., Hartmann, J., Lüpkes, C., Ehrlich, A., Garbrecht, T. and
18 Sellmann, M.: The Campaign MELTEX with Research Aircraft "POLAR 5" in the Arctic in
19 2008, Berichte zur Polar- und Meeresforschung/Reports Polar Mar. Res., 593, 3–85, 2009.

20 Bricaud, A., Morel, A. and Prieur, L.: Absorption by dissolved organic matter of the sea
21 Domains, (yellow substance) in the UV and visible, Limnol. Ocean.,26(1), 43–53, 1981.

22 Curry, J. A., Schramm, J. L. and Ebert, E. E.: Sea-ice albedo climate feedback mechanism, J.
23 Clim., 8(2), 240–247, 1995.Eicken, H., Grenfell, T. C., Perovich, D. K., Richter-Menge, J. A.
24 and Frey, K.: Hydraulic controls of summer Arctic pack ice albedo, J. Geophys. Res. C
25 Ocean., 109(8), C08007, doi:10.1029/2003JC001989, 2004.

26 Geldsetzer, T., Scharien, R. K., Yackel, J. J., Cheng, B. and Else, B. G. T.: Multipolarization
27 SAR for operational sea ice monitoring, Technical Report for POL-ICE 2006 2006-12-11.,
28 2006.

29 Gonzalez, R. C. and Woods, R. E.: Digital Image Processing, Second Edition, Prentice Hall
30 Inc., 2002.

Grenfell, T. C. and Perovich, D. K.: Seasonal and spatial evolution of albedo in a snow-ice-land-ocean environment, J. Geophys. Res., 109(C1), C01001, doi:10.1029/2003JC001866, 2004.

Hanesiak, J. M., Barber, D. G., De Abreu, R. A. and Yackel, J. J.: Local and regional albedo observations of arctic first-year sea ice during melt ponding, J. Geophys. Res., 106(C1), 1005, 2001.

Istomina, L. G., Heygster, G., Huntemann, M., Marks, H., Zege, E. P., Malinka, A. V., Prikhach, A. S. and Katsev, I. L.: The melt pond fraction and spectral sea ice albedo retrieval from MERIS data II: case studies and trends of sea ice albedo and melt pond fraction in the Arctic for years 2002-2011, Cryosph., 2015.

Istomina, L. G., von Hoyningen-Huene, W., Kokhanovsky, A. A. and Burrows, J. P.: The detection of cloud-free snow-covered areas using AATSR measurements, Atmos. Meas. Tech., 3(4), 1005–1017, doi:10.5194/amt-3-1005-2010, 2010.

Istomina, L., Nicolaus, M. and Perovich, D.: Spectral albedo of sea ice and melt ponds measured during POLARSTERN cruise ARK XXII/3 (IceArc) in 2012. PANGAEA Dataset., doi:10.1594/ PANGAEA.815111, 2013.

Jensen, J.: Introductory digital image processing: a remote sensing perspective, Third Edition, Prentice Hall Inc., 2008.

Kokhanovsky, A. a., Budak, V. P., Cornet, C., Duan, M., Emde, C., Katsev, I. L., Klyukov, D. A., Korkin, S. V., C-Labonnote, L., Mayer, B., Min, Q., Nakajima, T., Ota, Y., Prikhach, A. S., Rozanov, V. V., Yokota, T. and Zege, E. P.: Benchmark results in vector atmospheric radiative transfer, J. Quant. Spectrosc. Radiat. Transf., 111(12-13), 1931–1946, doi:10.1016/j.jqsrt.2010.03.005, 2010.

Lampert, A., Maturilli, M., Ritter, C., Hoffmann, A., Stock, M., Herber, A., Birnbaum, G., Neuber, R., Dethloff, K., Orgis, T., Stone, R., Brauner, R., Kässbohrer, J., Haas, C., Makshtas, A., Sokolov, V. and Liu, P.: The Spring-Time Boundary Layer in the Central Arctic Observed during PAMARCMiP 2009, Atmosphere (Basel)., 3(4), 320–351, doi:10.3390/atmos3030320, 2012.

Lehmann, P.: Geophysikalische Messungen für Nordostgrönland, Scientific report, Bremerhaven., 2012.

Nicolaus, M., Katlein, C., Maslanik, J. A. and Hendricks, S.: Sea ice conditions during the POLARSTERN cruise ARK-XXVI/3 (TransArc) in 2011, PANGAEA Dataset., doi:10.1594/PANGAEA.803312, 2012.

Perovich, D. K.: The Optical Properties of Sea Ice, Hanover (NH, USA) US Army Cold Reg. Res. Eng. Lab. Rep. 96-1. www.dtic.mil/cgi-bin/ GetTRDoc?AD=ADA310586, (May), 1996.

21

1 Perovich, D. K., Grenfell, T. C., Light, B., Elder, B. C., Harbeck, J., Polashenski, C., Tucker,
2 W. B. and Stelmach, C.: Transpolar observations of the morphological properties of Arctic
3 sea ice, J. Geophys. Res. C Ocean., 114(1), C00A04, doi:10.1029/2008JC004892, 2009.

4 Polashenski, C.: Attributing Change and Understanding Melt Ponds on a Seasonal Ice Cover,
5 181 pp., Darthmouth College, Hanover, New Hampshire., 2011.

6 Polashenski, C., Perovich, D. and Courville, Z.: The mechanisms of sea ice melt pond
7 formation and evolution, J. Geophys. Res., 117(C1), C01001, doi:10.1029/2011JC007231,
8 2012.

9 Press, W., Teukolsky, S., Vetterling, W. and Flannery, B.: Numerical Recipes: The Art of
10 Scientific Computing, Cambridge University Press., 1987.

11 Rösel, A., Kaleschke, L. and Birnbaum, G.: Melt ponds on Arctic sea ice determined from
12 MODIS satellite data using an artificial neural network, Cryosph., 6(2), 431–446,
13 doi:10.5194/tc-6-431-2012, 2012.

14 Scharien, R. K. and Yackel, J. J.: Analysis of surface roughness and morphology of first-year
15 sea ice melt ponds: Implications for microwave scattering, IEEE Trans. Geosci. Remote
16 Sens., 43(12), 2927–2939, 2005.

17 Scharien, R. K., Yackel, J. J., Barber, D. G., Asplin, M., Gupta, M. and Isleifson, D.:
18 Geophysical controls on C band polarimetric backscatter from melt pond covered Arctic first-
19 year sea ice: Assessment using high-resolution scatterometry, J. Geophys. Res. Ocean.,
20 117(C9), n/a–n/a, doi:10.1029/2011JC007353, 2012.

21 Schlundt, C., Kokhanovsky, A. A., von Hoyningen-Huene, W., Dinter, T., Istomina, L. and
22 Burrows, J. P.: Synergetic cloud fraction determination for SCIAMACHY using MERIS,
23 Atmos. Meas. Tech., 4(2), 319–337, doi:10.5194/amt-4-319-2011, 2011.

24 Schröder, D., Feltham, D. L., Flocco, D. and Tsamados, M.: September Arctic sea-ice
25 minimum predicted by spring melt-pond fraction, 4(May), 353–357,
26 doi:10.1038/NCLIMATE2203, 2014.

27 Schwarz, P.: Quantitative characterisation of sea ice melt stages in the Arctic by means of
28 airborne photographs, 114 pp., University of Trier., 2013.

29 Shindell, D. and Faluvegi, G.: Climate response to regional radiative forcing during the
30 twentieth century, Nat. Geosci., 2(4), 294–300, doi:10.1038/ngeo473, 2009.

31 Tschudi, M. A., Maslanik, J. A. and Perovich, D. K.: Derivation of melt pond coverage on
32 Arctic sea ice using MODIS observations, Remote Sens. Environ., 112(5), 2605–2614,
33 doi:10.1016/j.rse.2007.12.009, 2008.

1   Tynes, H. H., Kattawar, G. W., Zege, E. P., Katsev, I. L., Prikhach, A. S. and Chaikovskaya,
2   L. I.: Monte Carlo and Multicomponent Approximation Methods for Vector Radiative
3   Transfer by use of Effective Mueller Matrix Calculations, Appl. Opt., 40(3), 400,
4   doi:10.1364/AO.40.000400, 2001.

5   Warren, S. G. and Brandt, R. E.: Optical constants of ice from the ultraviolet to the
6   microwave: A revised compilation, J. Geophys. Res. D Atmos., 113(14), D14220,
7   doi:10.1029/2007JD009744, 2008.

8   Yackel, J., Barber, D. G. and Hanesiak, J. M.: Melt ponds on sea ice in the Canadian
9   Archipelago: 1. Variability in morphological and radiative properties, J. Geophys. Res.,
10   105(C9), 22049–22060 doi: 10.1029/2000JC900075, 2000. Zege, E. P., Ivanov, A. P. and
11   Katsev, I. L.: Image transfer through a scattering medium, Springer-Verlag, Heidelberg.,
12   1991.

13   Zege, E. P., Malinka, A. V., Katsev, I. L., Prikhach, A. S., Heygster, G., Istomina, L. G.,
14   Birnbaum, G. and Schwarz, P.: Algorithm to retrieve the melt pond fraction and the spectral
15   albedo of Arctic summer ice from satellite data, Remote Sens. Environ., 163, 153-164,
16   doi:10.1016/j.rse.2015.03.012, 2015.

17

1   Table 1. Datasets used for validation of the MPD algorithm

Campaign and year	Method	Ref.
Barrow 2009	In situ field campaign, fractions along a 200m transect	(Polashenski, 2011)
MELTEX 2008	Airborne measurements, supervised classification algorithm applied to geolocated quality assured aerial images	(Birnbaum et al., 2009; Schwarz, 2013)
NOGRAM-2 2011	Airborne measurements, supervised classification algorithm applied to geolocated quality assured aerial images	(Lehmann, 2012; Schwarz, 2013)
C-ICE 2002	In situ field campaign, visual estimation and fractions along 100m transects	(Scharien and Yackel, 2005)
HOTRAX 2005	Ship cruise, hourly bridge observations, visual estimation	(Perovich et al., 2009)
TransArc 2011	Ship cruise, hourly bridge observations, visual estimation	(Nicolaus et al., 2012)
POL-ICE 2006	In situ field campaign, fractions along a 200m transect	(R. Scharien, Sect. 3.2.1)

2

1 Table 2. Transect measurements of surface type fractions in the Canadian Arctic, POL-ICE

2 2006, where the relative surface type fractions are as follows: f_1 is the snow/bare ice, f_2 – melt

3 pond, f_3 – mixed cover, f_4 – overfrozen melt pond.

id	date_ut	time_ut	loc_y	loc_x	n	f_1	f_2	f_3	f_4
1	26-Jun-2006	15:00	74.73324	-95.10583	383	0.37	0.31	0.32	0.00
2	27-Jun-2006	0:00	74.732	-95.10324	400	0.23	0.41	0.36	0.00
3	28-Jun-2006	0:00	74.73164	-95.14458	395	0.21	0.57	0.22	0.00
4	28-Jun-2006	18:30	74.73079	-95.14778	401	0.24	0.54	0.22	0.00
5	2-Jul-2006	15:00	74.73015	-95.16151	398	0.35	0.26	0.39	0.00
6	4-Jul-2006	17:30	74.73102	-95.15971	400	0.37	0.31	0.32	0.00
7	5-Jul-2006	14:45	74.7304	-95.17052	400	0.24	0.41	0.35	0.00
8	6-Jul-2006	3:00	74.73097	-95.1729	400	0.22	0.41	0.38	0.00
9	6-Jul-2006	17:00	74.7309	-95.17329	400	0.31	0.30	0.40	0.00
10	9-Jul-2006	15:00	74.72987	-95.17271	400	0.38	0.06	0.38	0.19
11	10-Jul-2006	0:30	74.7301	-95.17448	400	0.30	0.09	0.61	0.00
12	11-Jul-2006	16:45	74.72998	-95.16605	400	0.33	0.22	0.46	0.00

4

1 Table 3. Integrated (320-950nm) albedo for various surface types and total obtained from
2 transect radiance measurements in Canadian Arctic, POL-ICE 2006, versus corresponding
3 retrieved broadband (400-900nm) albedo averaged within 5 km around the location. n is the
4 amount of measurements, f is the surface type fraction, α is the integrated albedo.

	SNOW/BARE ICE				MIXED				POND				RESULT
id	n	f	avg α	std α	n	f	avg α	std α	n	f	avg α	std α	Total α /retrieved
2	83	0.21	0.51	0.07	86	0.22	0.31	0.05	226	0.57	0.24	0.03	**0.31**/N/A
3	94	0.24	0.62	0.06	89	0.22	0.40	0.13	217	0.54	0.23	0.02	**0.36**/0.47
6	149	0.37	0.57	0.05	126	0.32	0.33	0.10	125	0.31	0.22	0.03	**0.38**/N/A
7	97	0.24	0.54	0.05	140	0.35	0.29	0.10	163	0.41	0.21	0.02	**0.32**/0.40
9	122	0.31	0.58	0.04	158	0.40	0.32	0.11	120	0.30	0.20	0.01	**0.36**/0.58
10	150	0.38	0.68	0.04	152	0.38	0.38	0.12	23	0.06	0.20	0.01	**0.46**/0.48
11	119	0.30	0.56	0.04	244	0.61	0.30	0.11	37	0.09	0.18	0.01	**0.37**/N/A
12	132	0.33	0.71	0.07	182	0.46	0.33	0.16	86	0.22	0.20	0.02	**0.43**/N/A
Combined			**0.60**	**0.08**			**0.33**	**0.12**			**0.21**	**0.03**	

5

26

1   Table 4. UTC time of aerial measurements (mpf and alb) and satellite overflights (sat) for

2   each day of available aerial measurements of MELTEX 2008 and NOGRAM 2011. Cases

3   with large time difference (greater than 1.5^h) between satellite and field measurements are

4   shown in red.

Date	26.05.2008	03.06.2008	04.06.2008	06.06.2008	07.06.2008	21.07.2011
alb	20:45-21:48	17:00-19:46	19:14-23:24	no drift,	17:08-20:17	no drift,
mpf	20:55-22:55	16:59-17:53	19:14-22:03	FI	17:56-19:22	MYI
sat	20:46	19:54	21:02		21:08	

5

6

27
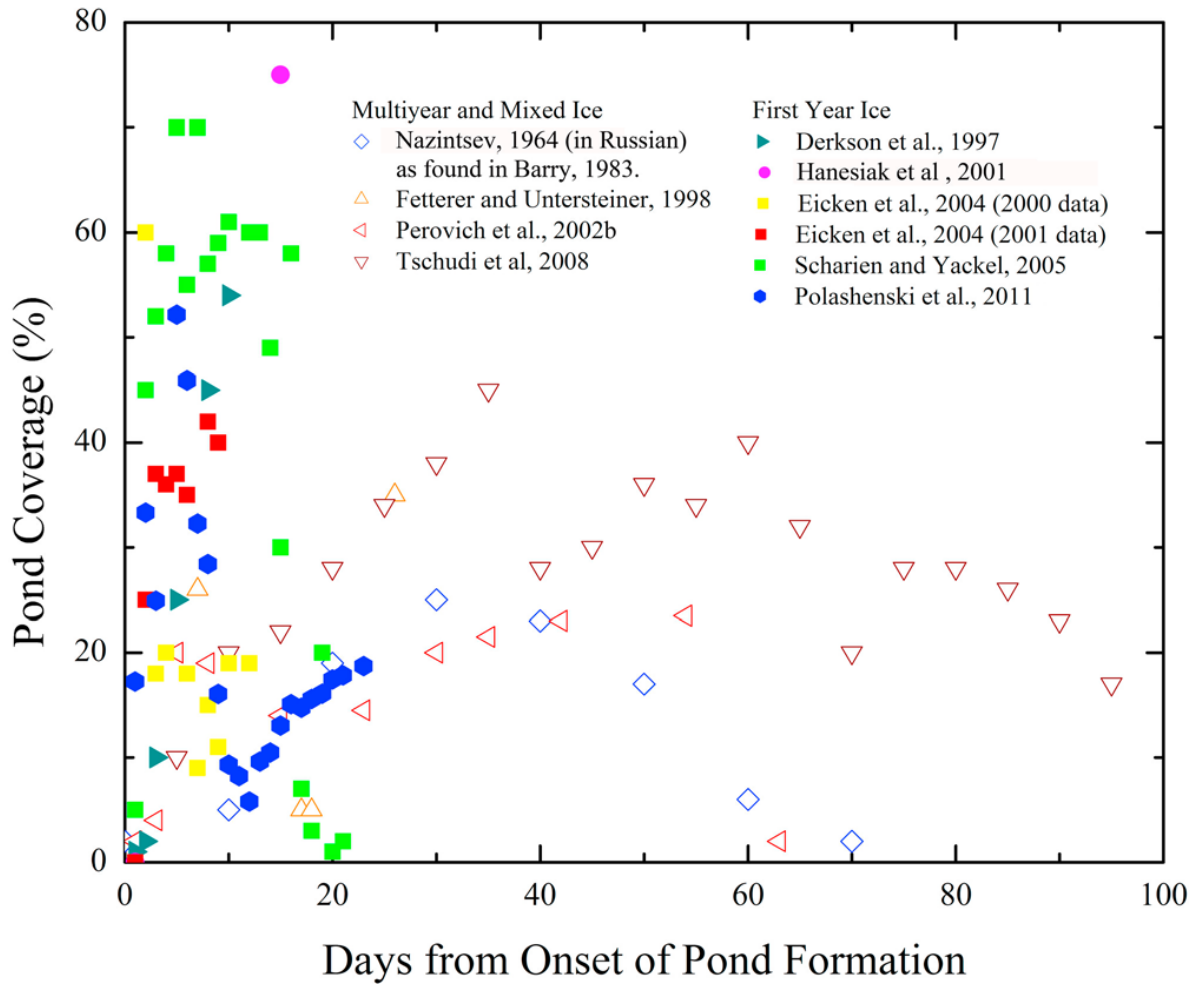
Figure 1. Pond coverage taken from various field campaigns (see legend) versus days from onset of ponding on first year ice (filled dots) and multiyear ice (empty dots). Melt onset proceeds rapidly to the MPF maximum on FYI with following pond drainage and moderate MPFs afterwards; on multiyear ice, the evolution of melt up to the melt maximum takes longer, the peak MPF value is lower and the MPF decrease is slower than that on FYI. Figure courtesy C. Polashenski.

28
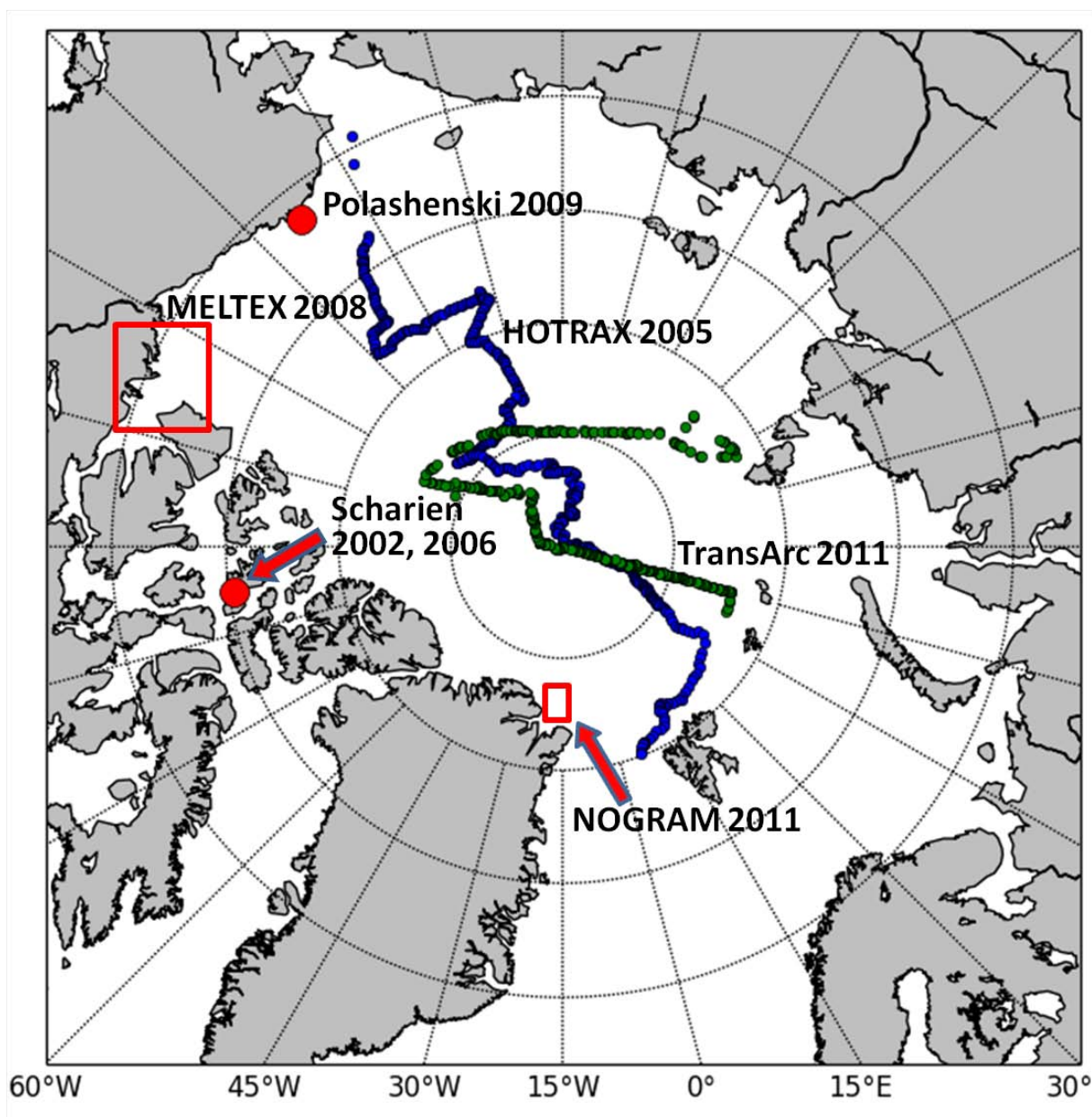
Figure 2. Schematic representation of the spatial distribution of the validation data. Red dots show the location of in situ field measurements; tracks – ship cruises, rectangles – approximate area of airborne measurements. The data includes FYI and MYI.

29
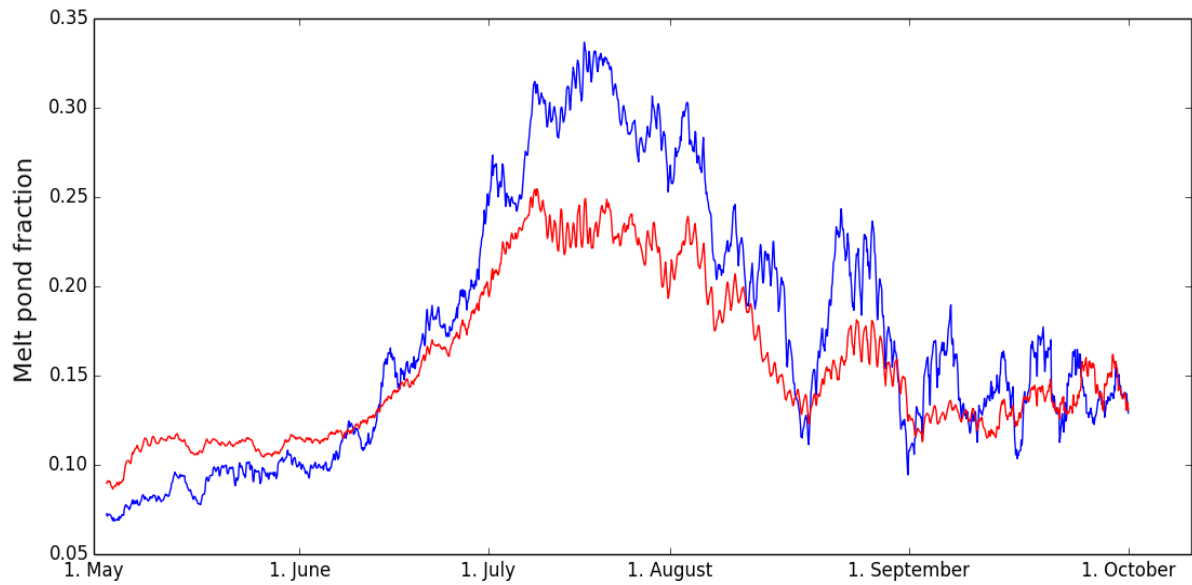
Figure 3. Swathwise comparison of the MERIS cloud mask used in the MPD retrieval to the AATSR cloud mask presented in (Istomina et al., 2010). The region covered is the Arctic Ocean to the north of 65°N (land masked out). All available swaths from May, 1, 2009 to September, 30, 2009 have been taken. Blue curve: MPF retrieved with MPD averaged in cloud free areas as seen by AATSR (reference or "perfect" cloud mask). Red curve: MPF retrieved with MPD averaged in cloud free areas as seen by MERIS (potentially cloud contaminated mask). The smoothing out effect of unscreened clouds is visible in the behavior of the red curve.

30

1

2

3
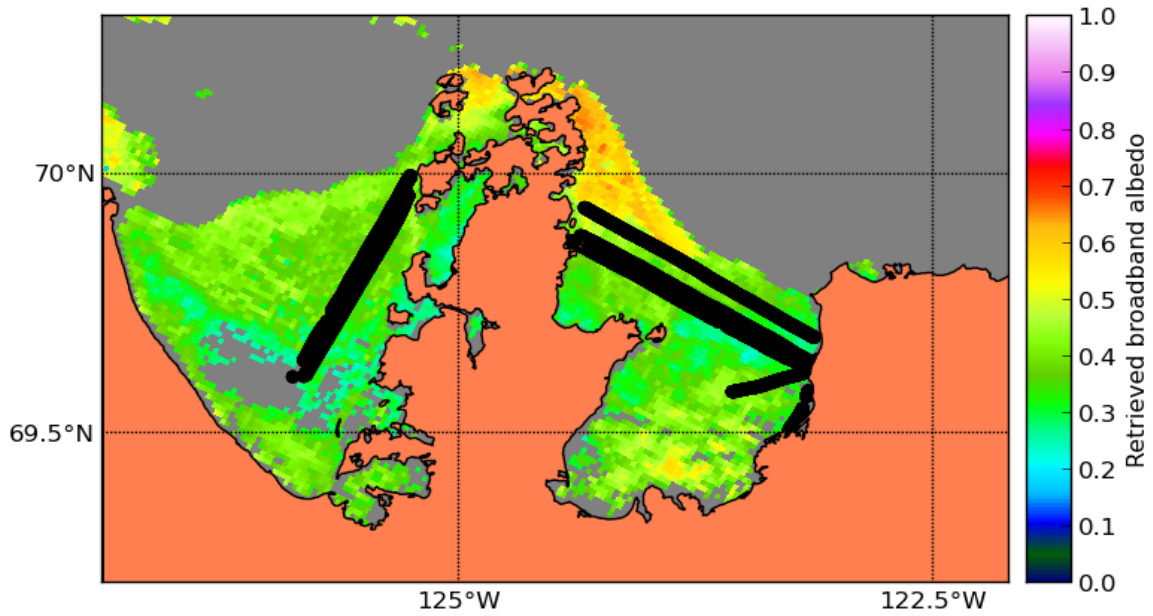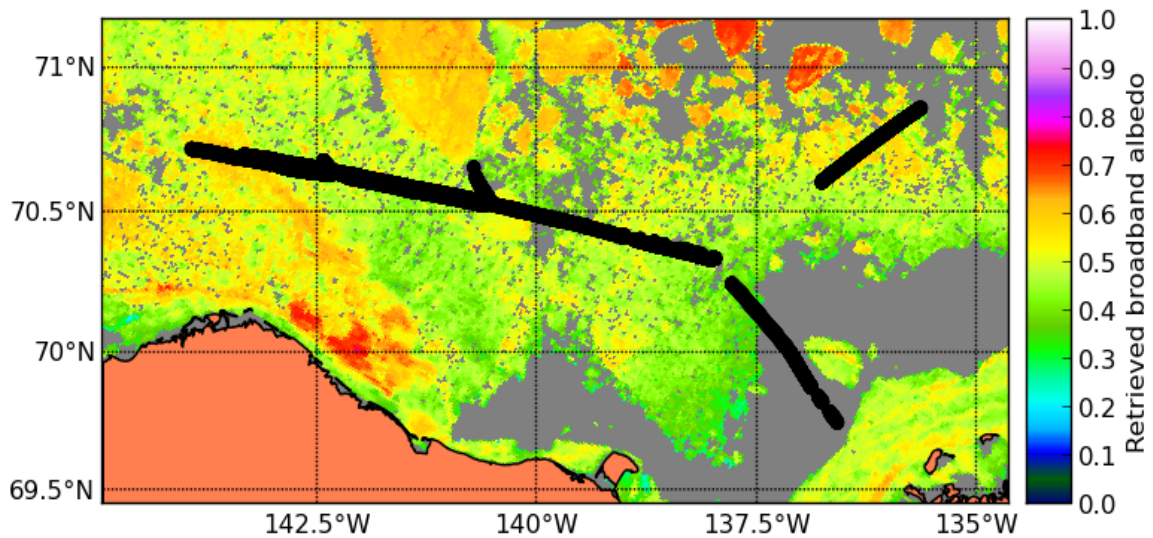
Figure 4. Examples of ice conditions present during MELTEX 2008 flights over landfast ice
on June 06, 2008 (top panel) and over separate ice floes of various sizes on June 04, 2008
(bottom panel). The black tracks depict the flight tracks with albedo measurements. The color
code illustrates the satellite retrieved broadband albedo. The background consists of the coral
filled landmask and grey filled data gaps due to cloud contamination or surface type other
than sea ice.

10

31

1

2

3
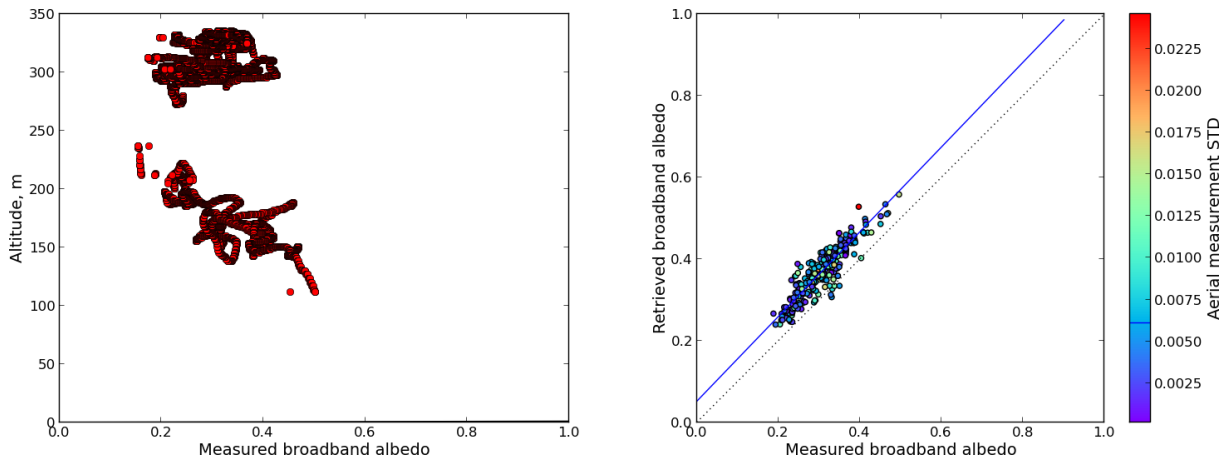
Figure 5. Altitude of the airborne broadband albedo measurements on June 06, 2008,
MELTEX campaign (left). Correlation between retrieved broadband albedo from satellite data
and measured broadband albedo over landfast ice (no drift) (flight track shown on the top
panel Figure 3). STD is calculated from all collocated aerial measurements for a given
satellite pixel. Only pixeös with STD smaller than the mean STD are used. N = 169, R = 0.84,
RMS=0.068.

10
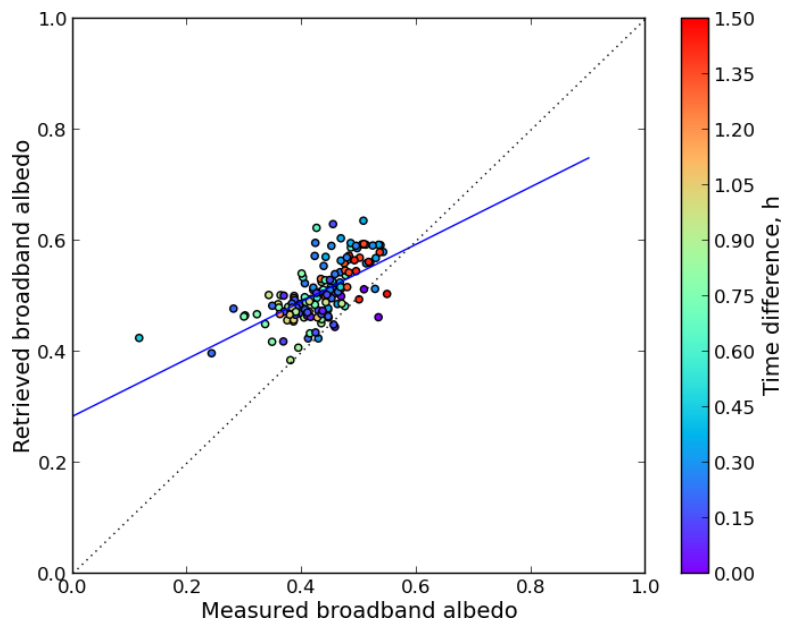
1

2 Figure 6. Correlation between broadband albedo retrieved from airborne measurements and
3 from a satellite overflight, respectively, for the June 04, 2008, MELTEX campaign (bottom
4 panel of Figure 3) with respect to time difference. N=147, R^2=0.39, RMS=0.089.
5

33
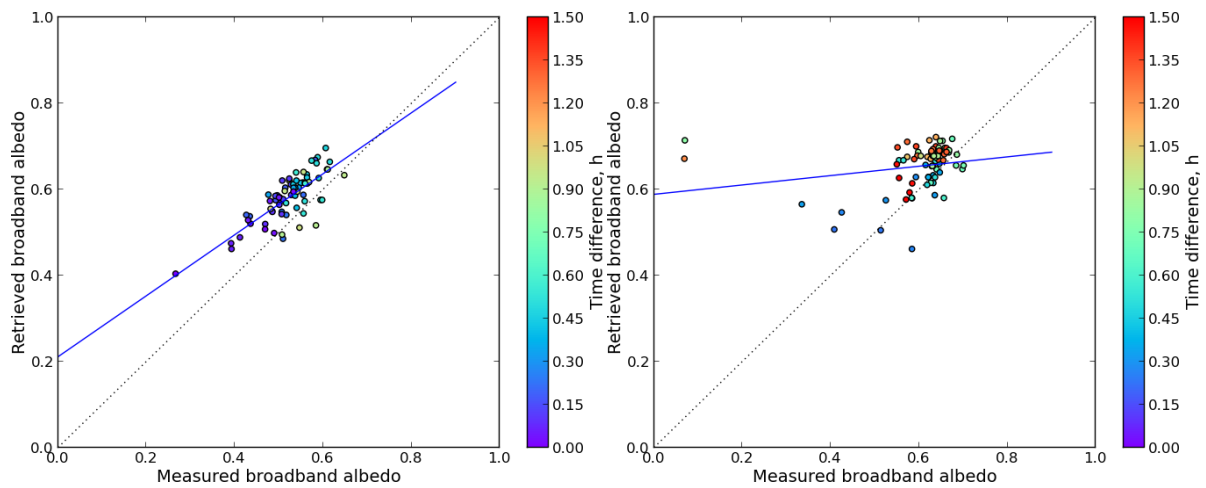
Figure 7. Correlation between broadband albedo retrieved from airborne measurements (MELTEX campaign) and from a satellite overflight, respectively, for the May 26, 2008 (left panel), N=73, R^2=0.61, RMS=0.07 and June 03, 2008, (right panel), N=78, R^2=0.05, RMS=0.121, with respect to time difference. The flight on June 03, 2008 features the greatest time difference to the satellite overflight, therefore most of the points have been discarded due to possible drift contamination.

34

1

2
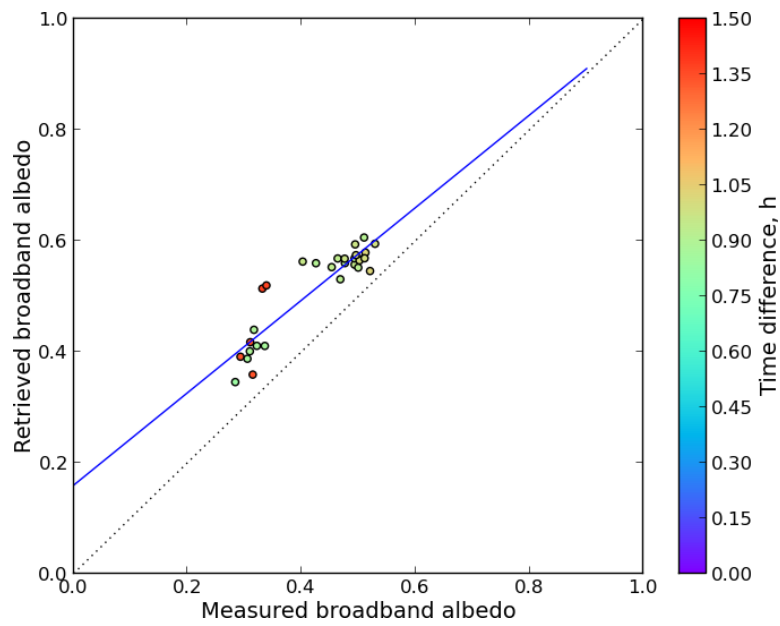
Figure 8. Correlation between broadband albedo retrieved from airborne measurements
(MELTEX campaign) and from a satellite overflight, respectively, for the June 07, 2008, with
respect to the time difference. N=30, R^2=0.82, RMS=0.096.

6

35

1

2
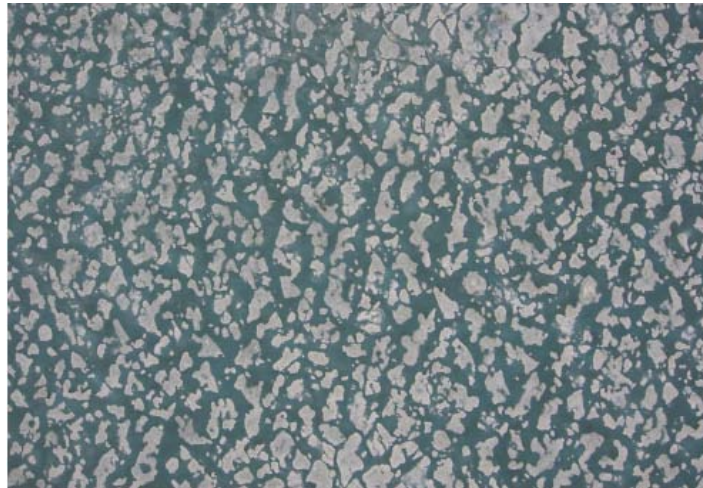
3 Figure 9. Example of aerial photo from MELTEX campaign in 2008, flight over landfast ice
4 on June 04, 2008. The image width is approximately 400 m. Only quality assessed images
5 were taken (see text for details).

6
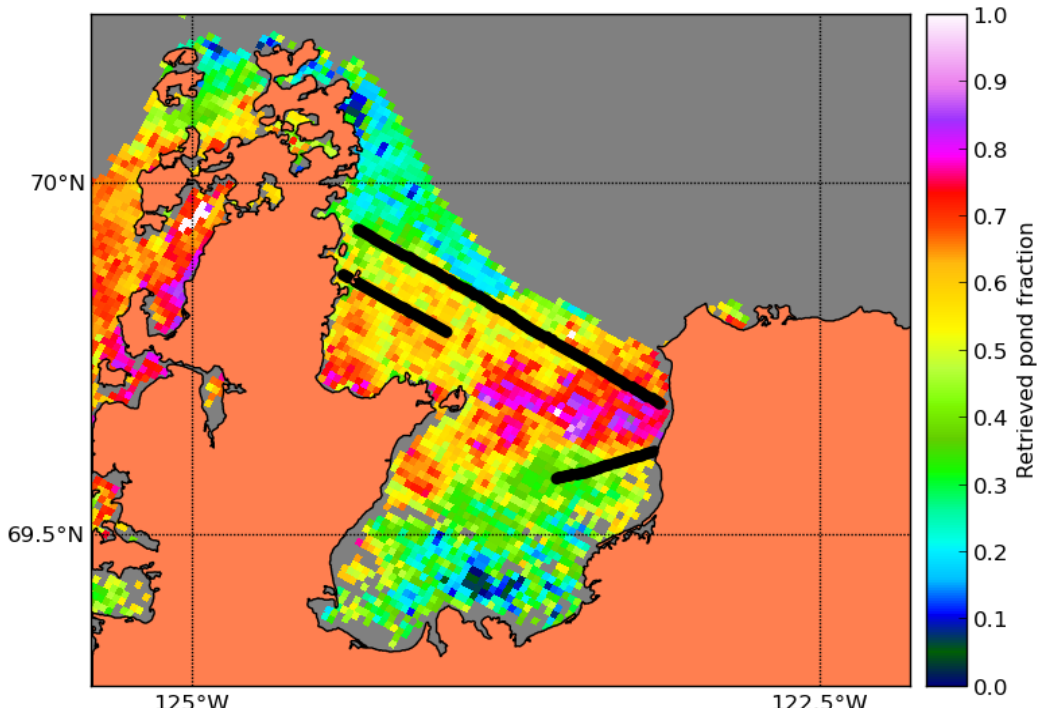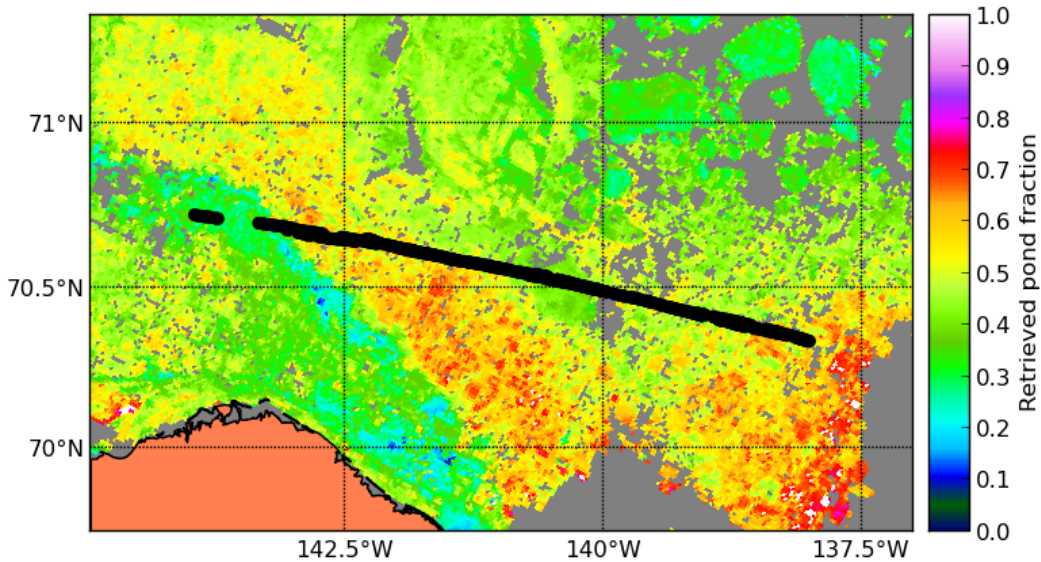
Figure 10. Examples of ice conditions present during MELTEX 2008 flights over landfast ice on June 06, 2008 (top panel) and over separate ice floes of various sizes on June 04, 2008 (bottom panel). Black dots: the flight track. The colored filled background: the satellite retrieved melt pond fraction. The background is the coral filled landmask and grey filled data gaps due to cloud contamination or surface type other than sea ice.

37

1

2
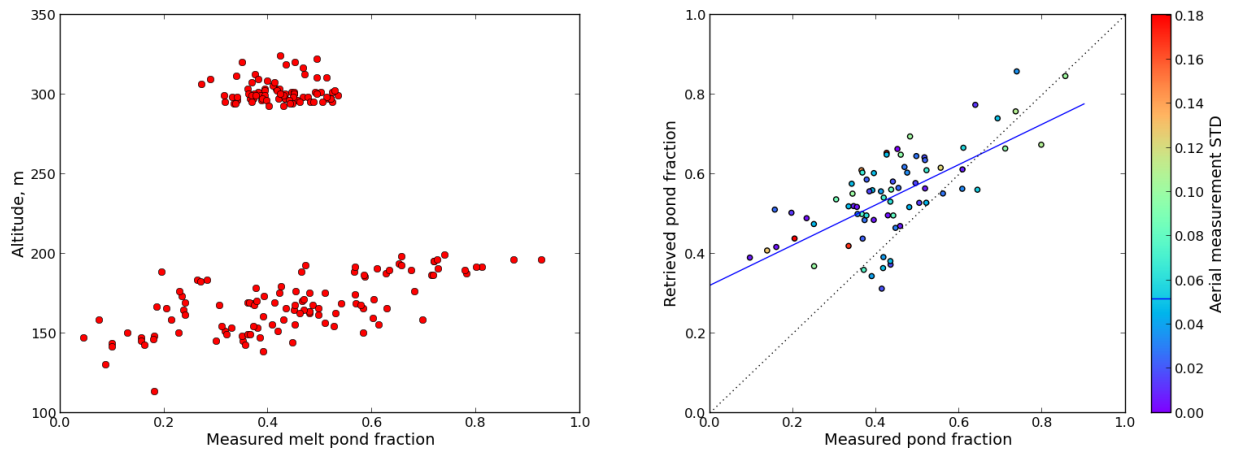
Figure 11. Altitude of the airborne melt pond measurements on June 06, 2008 (left). Correlation between retrieved melt pond fractions from satellite and airborne classified MPF over landfast ice with no drift (right), June 06, 2008 during MELTEX campaign. The flight track shown on the top panel Figure 9. N=48, R^2=0.36, RMS=0.154.
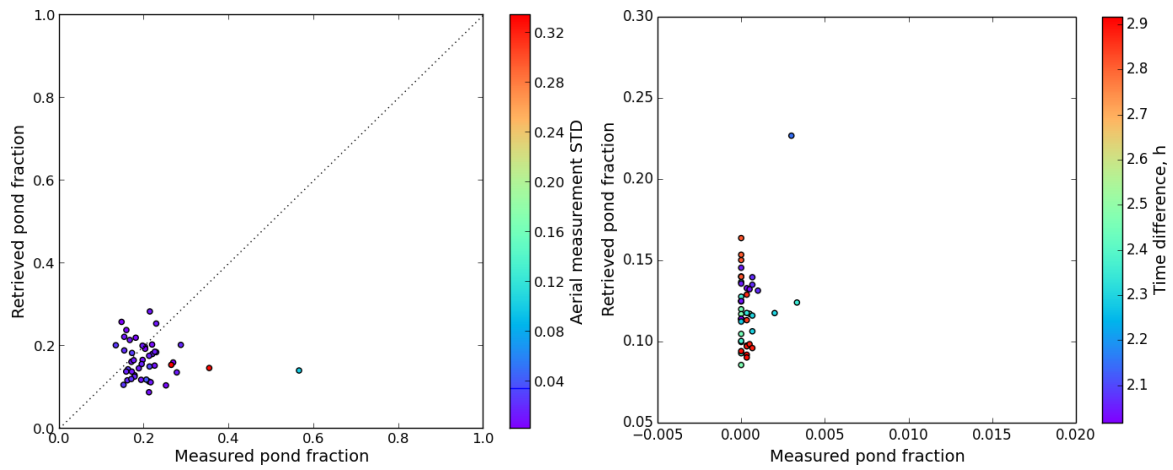
Figure 12. Correlation between retrieved melt pond fractions from satellite and airborne classified MP over MYI (no drift, ice pack), July 21, 2011, NOGRAM-2, 2011, campaign north of Greenland (left). N=40, R^2=0.004. RMS = 0.065 and over FYI, June 03, 2008, MELTEX 2008 (large floes but drift + large time difference) (right), N=44, R^2=0.13, RMS = 0.123. See Figure 2 for locations of the NOGRAM-2 and MELTEX campaigns.

39
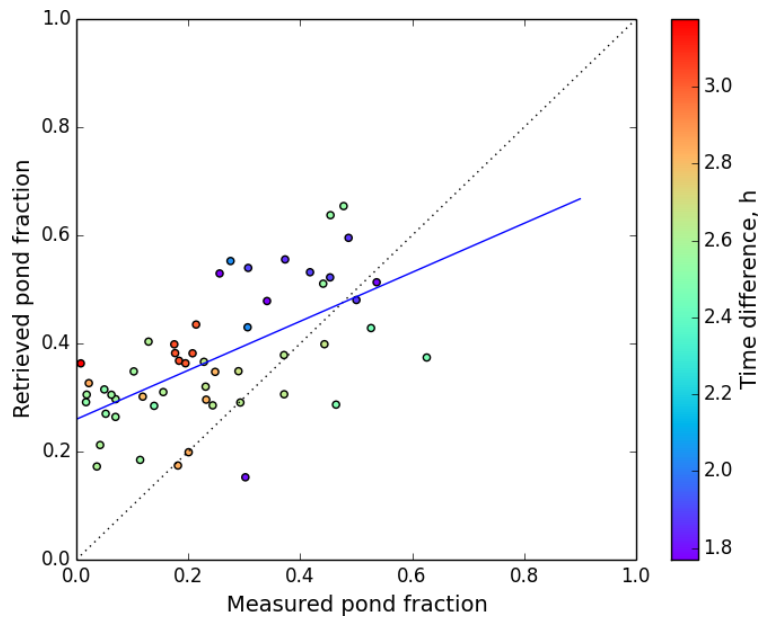
Figure 13. Correlation between retrieved melt pond fractions from satellite and airborne classified MP over FYI, possible drift, June 07, 2008, MELTEX2008, Beaufort Sea. This case features larger ice floes than flights on June 04 or May 26, 2008. N=53, R^2=0.37, RMS = 0.179.

1

2
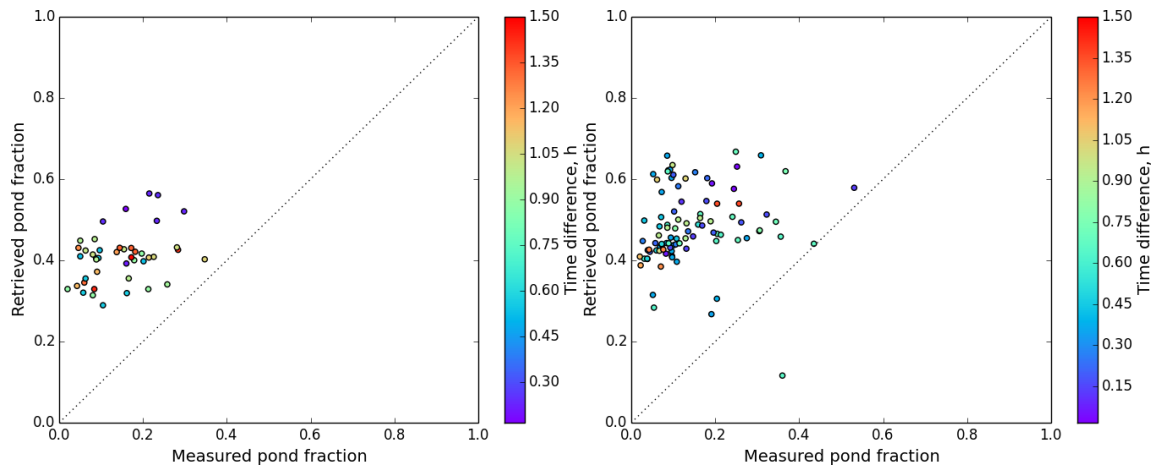
Figure 14. Retrieved melt pond fractions from satellite versus airborne classified MP over FYI, possible drift, May 26, 2008 (left panel), N=44, R^2=0.13, RMS=0.274, and June 04, 2008 (right panel, the flight track is shown in Figure 9, bottom panel), Beaufort Sea, N=93, R^2=0.02. RMS=0.361. Both cases feature brash ice with subpixel ice floes which are covered not with white ice, but with blue ice (sea ice without the scattering layer), which has spectral response similar to MP within the VIS and IR spectral range.
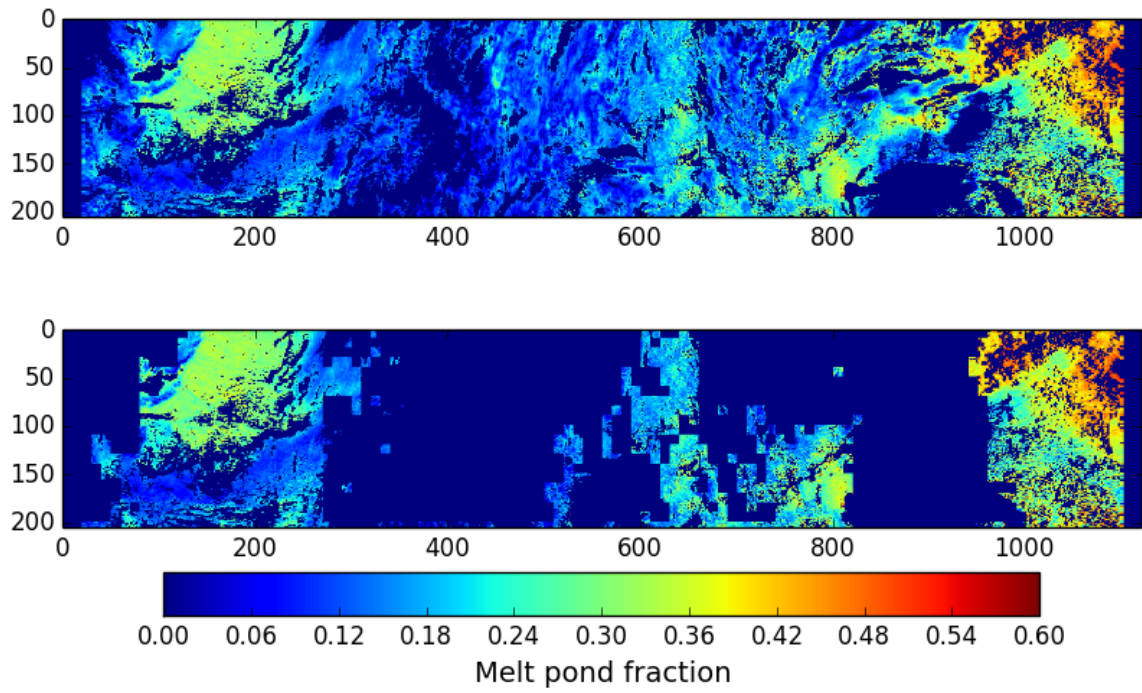
Figure 15. Example of a spatial dynamic cloud filtering for MERIS swath data: original swath subset with the cloud filters from (Zege et al., 2015) applied (top panel), same swath subset after applying the dynamic spatial filter (see text).

1

2

3 Figure 16. An example image made from the bridge of RV "Polarstern" during the TransArc
4 2011 (ARK XXVI3) on the 4th of September 2011 within the course of ASPeCt observations.
5 The pond fraction estimated during the cruise is 0.5. The satellite retrieved pond fraction for
6 such cases will be significantly smaller because of high albedo of frozen over snow covered
7 ponds. Image source (Nicolaus et al., 2012).
8

1

2
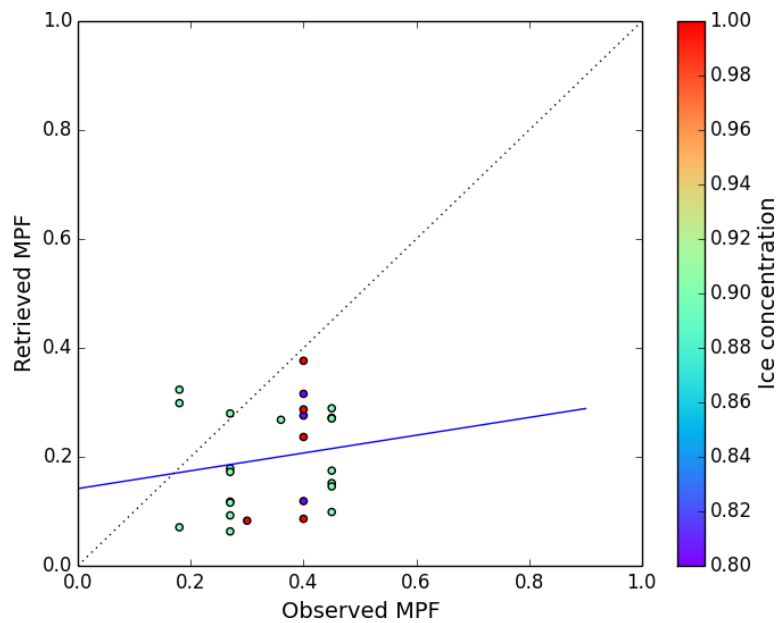
3 Figure 17. Retrieved MPF versus observed MPF from the hourly bridge observations during

4 TransArc2011, 04 August 2011 – 6 October 2011. Swath data, no temporal averaging, 15km

5 satellite average around the in situ point. All but one point is FYI. Corrected for ice

6 concentration. Underestimation may be connected to undocumented presence of melted

7 through or overfrozen ponds at the end of the melt season (see Figure 16). R^2=0.026,

8 RMS=0.19, N=26.

9

44

1

2
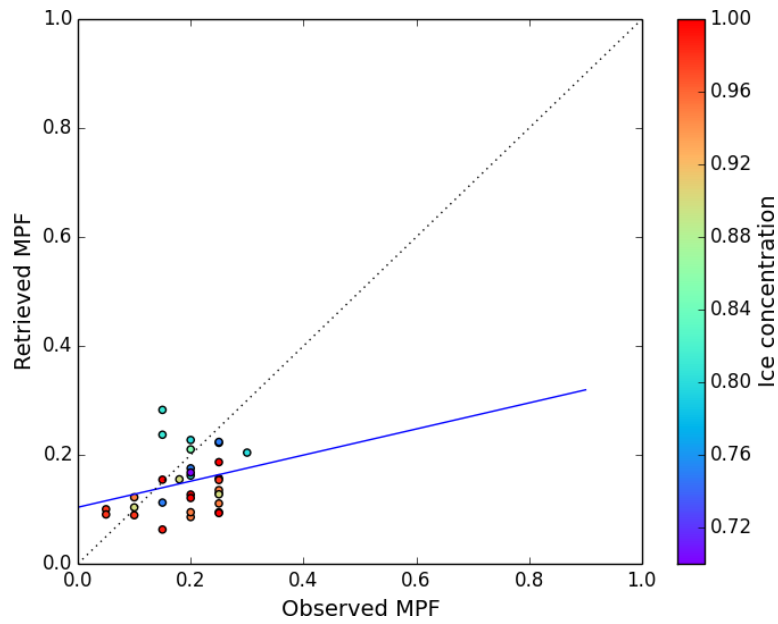
3 Figure 18. Retrieved MPF versus observed MPF from the hourly bridge observations during

4 HOTRAX2005, 19 August – 27 September 2005. Swath data, no temporal averaging, 15km

5 satellite average around the in situ point. No information on ice type. Corrected for ice

6 concentration. Underestimation may be connected to undocumented presence of melted

7 through or frozen over ponds at the end of the melt season. R^2=0.067, RMS=0.084, N=32.

8

45

1
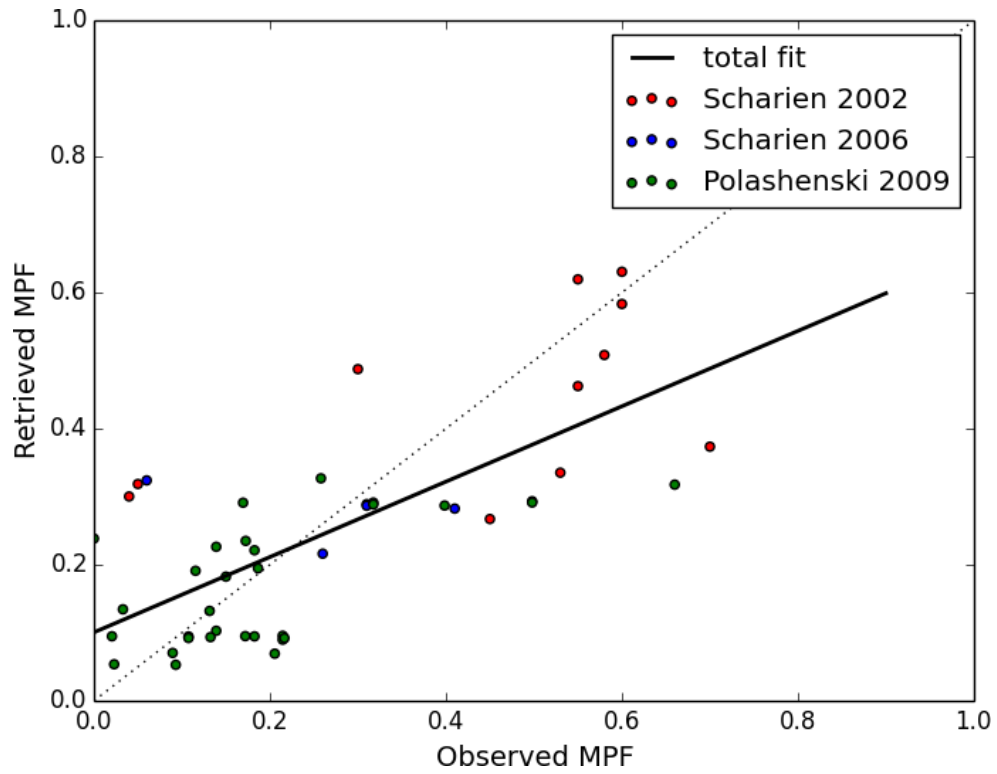
2

3

4   Figure 19. Three in situ campaigns on landfast ice: Scharien 2002 (red dots), Scharien 2006

5   (blue dots) and Polashenski 2009 (green dots). Total point number N = 47, RMS = 0.14, R^2 =

6   0.52. The overestimation of the low MPF may be connected to unscreened thin clouds which

7   depending on the illumination-observation geometry may appear darker than the ice and

8   therefore cause higher retrieved MPF.

9

46

Melt pond fraction and spectral sea ice albedo retrieval from MERIS data II: case studies and trends of sea ice albedo and melt ponds in the Arctic for years 2002-2011

L. Istomina[1], G. Heygster[1], M. Huntemann[1], H. Marks[1], C. Melsheimer[1], E. Zege[2], A. Malinka[2], A. Prikhach[2] and I. Katsev[2]

[1]{Institute of Environmental Physics, University of Bremen, Bremen, Germany}

[2]{B.I. Stepanov Institute of Physics, National Academy of Sciences of Belarus, Minsk, Belarus}

Correspondence to: L. Istomina (lora@iup.physik.uni-bremen.de)

Abstract

The spatial and temporal dynamics of melt ponds and sea ice albedo contain information on the current state and the trend of the climate of the Arctic region. This publication presents a study on melt pond fraction (MPF) and sea ice albedo spatial and temporal dynamics obtained with the Melt Pond Detection (MPD) retrieval scheme for the Medium Resolution Imaging Spectrometer (MERIS) satellite data. This study compares sea ice albedo and MPF to surface air temperature reanalysis data, compares MPF retrieved from the Moderate Resolution Imaging Spectroradiometer (MODIS), and examines albedo and MPF trends. Weekly averages of MPF for 2007 and 2011 showed different MPF dynamics while summer sea ice minimum was similar for both years. The gridded MPF and albedo products compare well to independent reanalysis temperature data and show melt onset when the temperature gets above zero, however MPD shows an offset at low MPFs of about 10% most probably due to unscreened high clouds. Weekly averaged trends show pronounced dynamics of both, MPF and albedo: a negative MPF trend in the East Siberian Sea and a positive MPF trend around Queen Elizabeth Islands. The negative MPF trend appears due to a change of the absolute MPF value in its peak, whereas the positive MPF trend is created by the earlier melt onset,

1

with the peak MPF values unchanged. The MPF dynamics in the East Siberian Sea could indicate a temporal change of ice type prevailing in the region, as opposed to the Queen Elizabeth Island, where MPF dynamics react to an earlier seasonal onset of melt.

1   Introduction

In the last few decades, the sea ice extent (defined as the total area with at least 15% of ice cover) and area of multiyear ice (MYI) has been declining at even faster rate than that of the total perennial ice (Comiso, 2012). This tendency of the sea ice towards thinner and younger ice has a strong impact on the energy balance of the system atmosphere-sea ice-ocean (Perovich et al., 2011; Wang et al., 2014) where 96% of the total annual solar heat input through sea ice occurs during the melt season from May to August (Arndt and Nicolaus, 2014). The above mentioned effects are of importance within the context of a changing Arctic due to the sensitivity of the regional climate balance and its importance for the global climate (Shindell and Faluvegi, 2009).

The extent of the Arctic sea ice cover has a pronounced seasonal cycle with the maximum typically in March (in February in 2015) and the minimum in September. The main feature of the sea ice in summer is the presence of melt ponds. Knowing their spatial and temporal dynamics during the melt season and over several years can help improve understanding of the current state and trends of the energy balance in the region. The sea ice extent has been showing a general declining trend ever since the beginning of continuous satellite observations in the late 1970s. This decline has been stronger for the September minimum than for the March maximum (Cavalieri and Parkinson, 2012; Stroeve et al., 2011). The decline of the minimum sea ice extent has become very significant since 2007: in September 2007, the minimum sea ice extent of 4.15million km^2 was about 39% below the average minimum of 1981-2000, and in 2012 the minimum (3.41 million km^2) was 49% below the 1981-2000 average (Perovich et al., 2012). While the minima of Arctic sea ice extent were less dramatic in the other years since 2007, it has to be noted that all minima after 2007 were below all yearly minima observed before 2007 (since beginning of satellite observations). What is the role of melt ponds in the above mentioned yearly dynamics of the sea ice cover?

2

The clear connection between the area of melt ponds in spring and sea ice extent during the sea ice minimum in autumn is highlighted in Schröder et al., (2014).

The temporal dynamics of melt can be subdivided into 4 stages (Eicken et al., 2002). Stage 1 occurs after the onset of positive air temperatures and is characterized by widespread ponding and lateral melt water flow. During the stage 2 both the surface albedo and MPF decrease due to removal of snow cover and due to pond drainage. During the stage 3, as the meltwater penetrates deeper into the ice, the pond coverage continues to evolve and MPF to grow. Stage 4 corresponds to freeze-up. This publication is dedicated to the application of the algorithm to retrieve MPF and sea ice albedo described and validated in the companion publications (Istomina et al., 2015; Zege et al., 2015). As the Melt Pond Detection (MPD) retrieval does not see separate ponds, but detects the spectral signature of melt ponds in the measured top-of-atmosphere signal, the retrieved MPF dynamics will somewhat deviate from above mentioned stages of melt observed in the field. The reason for this deviation is the ambiguity of the top-of-atmosphere signal, where e.g. the spectrum of melting sea ice (before stage 1) can be represented as a linear mixture of pond spectrum and non-melting ice spectrum, as can be seen from field spectra in e.g. Istomina, Nicolaus and Perovich et al., (2013). The problem is addressed in MPD by setting boundary conditions on optical parameters given in Eq. 18 in Zege et al., (2015). However, as the MPD uses only a limited amount of spectral bands in the VIS and NIR, surfaces which are similar in these channels may all be retrieved as MPF, e.g. submerged ice, blue ice and water saturated ice without yet actual meltwater on it. This may introduce a bias in the MPF product (not sea ice albedo), however, it does not imply limitations on the usage of the MPD product for the studies of radiative balance and global circulation models. Another source of bias of the MPD product are the unscreened thin clouds.

All available Medium Resolution Imaging Spectrometer (MERIS) reduced resolution data for the Arctic summers from 2002 to 2011 are processed and compiled in lower resolution in daily and weekly averages to increase the coverage and quality of the data. As the temporal evolution of the MPF and the surface albedo is naturally correlated with the evolution in air temperature at the surface, a comparison to National Centers for Environmental Prediction (NCEP) reanalysis temperature data for various ice types was performed to check the performance of the algorithm. This has been done for extended periods of time (over the

3

whole summer); also, in the context of the above mentioned connection of the MPF and sea ice extent, the MPF dynamics have been studied for the two years 2007 and 2011 and also compared to the data by Rösel and Kaleschke, (2012) for selected cases. The performed comparisons showed clear agreement both to reanalysis data and to the MPF by Rösel and Kaleschke, (2012).

The manuscript is structured as follows: Section 2 is dedicated to the comparison of the MPF and albedo data to the reanalysis air temperature for various locations . Global applications of the MPD algorithms over the whole MERIS dataset (2002-2011) are given in Section 3. There the weekly averages for 2007 and 2011 are analyzed (Sect. 3.1), for these cases a comparison to another MPF retrieval is performed (Sect. 3.2), trends of MPF (Sect. 3.3) and sea ice albedo (Sect. 3.4) are presented. The conclusions are given in Section 4.

2   Comparisons between surface air temperature and time series of MPF and albedo: Case studies of FYI and MYI

The processed swath MERIS Level 1b data obtained with the MPD algorithm as described in the companion publications (Istomina et al., 2015; Zege et al., 2015) have been gridded daily into the 12.5 km polar stereographic grid (the so-called National Snow and Ice Data Center (NSIDC) grid) with the criterion of more than 50% valid pixels (both spatially and temporally) within a grid cell to produce a valid grid cell. The standard deviation of such a mixed spatial and temporal average is also provided. Thus, the resulting NetCDF file contains four datasets: MPF, broadband albedo and their STDs. On average, there were around 13 overflights per day, with the density of overlapping swaths highest at about 80°N latitude. Even from a single overflight, there are at least 100 up to about 1000 data points for averaging into a single grid cell. Assuming a stable retrieval and low variations within a single day, the STD gives information about the spatial variation of MPF and broadband albedo within the grid cell. This kind of averaging does not provide a guarantee of a valid data point for every single day and grid point. The gridding method with a threshold on the amount of cloud free pixels allowed to form a valid grid cell assists with cloud screening because it does not allow partly screened out clouds or potentially unscreened cloud edges to appear in the end product. However, since the Arctic is one of the most cloud covered regions with up to 80% cloud cover throughout the year (Serreze and Barry, 2005), some of unscreened clouds will still

4

affect the gridded product. The amplitude of this effect tends to be the greatest (up to 15% MPF bias) before melt onset as it is the most challenging to separate clouds and bright snow/sea ice. Later in the season the surface becomes darker due to melt, which aids the cloud screening, and the bias on MPF and albedo introduced by unscreened clouds decreases.

The weekly resolution has been obtained by averaging the gridded daily product. As in the case of daily resolution, a weekly averaged grid cell is obtained from no less than 50% of valid (cloud free) pixels. Should a given grid cell contain more than 50% of invalid pixels, it is assigned not a number value. No weight or threshold on STDs is applied. The resulting STD is then written into the resulting NetCDF file together with the averaged value for the broadband albedo and MPF.

These weekly averages have a much higher data density since there is a higher probability for the satellite to observe cloud free areas within one week than it is the case for one day.

The essential difference in daily and e.g. weekly averages is the data coverage due to cloudiness and smoothness of the resulting product. This is why the gridded product has been used for case studies and data analysis on the Arctic scale. In order to illustrate the feasibility of the algorithm on FYI and MYI, time sequences over the summer 2009 have been produced for Beaufort Sea with mainly FYI and North Greenland with mainly MYI (Figure 1).

For this study, the daily averaged product was taken in the area 75N, 155W (Beaufort Sea) and 84.5N, 35W (North Greenland) and it was compared to the time sequence of daily averaged air temperature at the surface (0.995 sigma level) from NCEP reanalysis data (Kalnay et al., 1996). The difference between melt evolution in the selected location is mainly that melt onset happens about a month earlier in lower latitudes: beginning of June on FYI as opposed to beginning of July for MYI. Then, due to FYI roughness being much less than that of MYI, the maximum MPF on FYI can be about 4 times higher than that on MYI (maximum melt 0.2 on MYI as opposed to up to 0.8 on FYI, Figure 1 in Istomina et al., (2015)). While the melt onset occurs rapidly on both ice types, the later stage of melt - drainage of melt ponds - happens much sooner on FYI than on MYI. On MYI, this stage is generally substituted with MPF decrease due to freezing and snowfall events. One more difference between the two chosen locations is the sea ice concentration: for the MYI the ice concentration stays very high throughout the whole summer, whereas for the FYI region the

5

1   effect of ice concentration and also ice drift (in the swath data for consecutive days separate

2   floes and their drift is clearly visible) can affect the time sequence analysis, affecting the

3   noisiness of the retrieved values.

4   Overall, the comparison of the retrieved MPFs and albedos to the surface air temperature

5   (Figure 2) shows a clear connection between these during the melt onset: as soon as air

6   temperature assumes constantly positive values, sea ice albedo drops down and MPF

7   increases abruptly. For both FYI and MYI the maximum MPF is around 0.35, with melt onset

8   happening in the beginning of June for FYI and beginning of July for MYI. This corresponds

9   to the knowledge about melt onset and dynamics from field measurements (Figure 1 in

10 Istomina et al., (2015)). The evolution of melt on MYI follows the air temperature dynamics

11 and is ongoing till first snowfalls and freezing temperatures around mid August. The FYI

12 region, however, is closer to the ice edge and therefore features greater range of ice

13 concentrations within the study area. As a result, the corresponding curve appears noisier and

14 interrupts with the area becoming ice free starting 1st of August. For periods before melt

15 onset, the retrieved MPFs range from 0% to 10-15% with relatively high albedos; both might

16 be the effect of unscreened clouds which tend to increase retrieved pond fraction in case of

17 small true pond fraction and decrease it in case of high true pond fractions. The difference of

18 the sea ice type is also visible in the albedo values before the melt onset (Figure 2): higher

19 albedo of 90%for MYI region and lower albedo of about 80%) for the coastal region of

20 Beaufort Sea. For MPF before melt onset, the effect of subpixel ice floes and greater open

21 water fraction as compared to the MYI region may have caused the difference in MPF offset

22 with respect to expected value near zero before melt (Figure 2).

23 **3   Temporal and spatial analysis over the whole MERIS dataset**

24 This chapter presents the main highlights of the processed MERIS data for 2002-2011.

25 Weekly averages have been used for this study due to better data coverage; therefore the

26 shown trends are produced with the weekly resolution.

27 The most striking and characteristic stage of the melt season is the melt onset and the first

28 stage of melt evolution. Such dynamics are ice type specific, e.g. on FYI this is the rapid melt

29 pond formation followed by a rapid drainage, during which the MPF changes drastically up

30 and down within a scale of days to weeks. MYI features later (starts in July) and slower melt

6

onset, less extreme pond fractions with the absence of rapid melt evolution stages. The pond fractions in the melt maximum on MYI are close to pond fractions of the melt evolution (after melt onset and drainage) on FYI. Thus, the difference of MPF on FYI and MYI is most prominent in June. Therefore in this work we study the temporal variation of MPF and albedo for June of each year of the available MERIS dataset.

3.1 Weekly averages of June 2007 and 2011: how the record ice minimum in 2007 started

It is interesting to compare the evolution of melt ponds right after the onset of melt for the record sea ice minimum in 2007 and a similar one by the ice minimum extent year 2011, to see how the patterns of melt changed within these 5 years to reach the same resulting ice extent during the sea ice minimum. In Figure 3 the evolution of the MPFs from the last two weeks of May up to first two weeks of September 2007 and 2011 is shown. The onset and the melt stage 1 occur in the fourth week of May at the shore of Beaufort Sea (2007) and East-Siberian Sea (2011).

The melt stage 1 during the first week of June has much more local character in 2011 than in 2007, being centered near point Barrow and the shore of Beaufort Sea, as opposed to 2007 when the melt onset began already at a more global scale. The second week of June 2007 featured drastic melt which corresponds to the last phase of melt stage 1 with MPF values up to about 50% in the Beaufort Sea and the western part of the FYI covered Arctic Ocean (top row in Figure 4), whereas in 2011 the situation was more or less stable relative to the first week of June.

In the third and the fourth week of June 2011 large scale melt started (third week of June 2011, one week delay as compared to June 2007), but it is centered around the Queen Elizabeth Islands. The fourth week of June 2011 shows that melting spreads from there over the Eurasian Arctic Ocean, whereas in 2007 at this time these areas have already experienced the maximum of melt and are now draining (melt stage 2). MYI areas to the north of Greenland and Queen Elizabeth Islands for both years display the melt stage 1, which continues in July. The relatively high MPFs throughout the whole Arctic Ocean are interrupted with lower air temperatures in the Eurasian Arctic in the second week of July

7

2007 (bottom row in Figure 4). The lower air temperatures are evident in the time sequence of daily averaged NCEP air temperatures (0.995 sigma level) and MPFs (Figure 5) for both years for the characteristic location in the Barents Sea, where lower MPFs are observed in the second week of July 2007 as compared to 2011 (100 km average around 85°N, 65°E). A reference location north to the Queen Elizabeth Islands is also shown in Figure 5 (100 km average around 83°N, 110°W). The locations of the two sites are shown with yellow square tags tagged "E" and "W" respectively in Figure 1. The differences in the MPFs for the second week of June and second week of July 2007 and 2011 are summarized in Figure 4.

The rest of July and first two weeks of August feature similar melt evolution (melt stage 3) with occasional freezup and melt (Figure 3). The frequent freezups and snowfalls caused the MPF decrease at the northernmost latitudes in the last two weeks of August of both 2007 and 2011, while the melt ponds were still present closer to the ice edge of the Arctic ocean (also can be seen in Figure 5). The MPF decreases (melt stage 4) overall throughout the Arctic Ocean (according to the air temperature, the ponds are frozen over and most probably snow covered) in the first two weeks of September of both 2007 and 2011.

To conclude: the years 2007 and 2011 feature different times of various melt stages onset and also different spatial patterns of MPFs, however the ice extent near the ice minimum is similar. The most prominent feature is the rapid and large scale melt in the second week of June 2007 associated to the melt stage 1 before transition into drainage, which was not reproduced in 2011. This feature seems to be compensated by smaller MPFs in the first two weeks of July 2007, whereas the MPFs during the same time period in 2011 again do not reproduce this feature (Figure 4). This kind of opposite temporal MPF dynamics (2007) produces the same effect as an evolution of melt uniform in time (2011). The analysis of MPF time sequences (Figure 5) shows only a moderate (about 15%) MPF difference during the first two weeks of July between the comparison years 2007 and 2011. However, even moderate MPF values over a large area and longer period in 2011 (Figure 4) produce a drastic effect on the minimum ice extent similar to the short but extreme MPF peak in June 2007. For both 2007 and 2011, the areas of highest MPFs throughout the melt season are ice free at the time of ice minimum (1st and 2nd weeks of September, Figure 3). This conclusion on connection between MPF and sea ice extent during the ice minimum agrees well with the findings of Schröder et al., (2014).

8

3.2 Comparison to MPF from MODIS data (Rösel et al., 2012)

An unusual temporal and spatial dynamics of melt ponds in the Arctic Ocean in 2007 and 2011 has been initially discussed by Rösel and Kaleschke, (2012) based on MODIS data and the melt pond retrieval algorithm described in Rösel et al., (2012). It is interesting to compare these independent data obtained from a different sensor and retrieval method to the MPD MPF, and in case of agreement to confirm the unusual melt pond dynamics for the 2007 and 2011 summers.

For this comparison, two examples presented in Rösel and Kaleschke, (2012) are taken: 8 day composites starting on June 18, 2007 and June 18, 2011. These are the cases of prominent difference in melt pond patterns in 2007 and 2011. In order to compare the two datasets, the 8 day composites from MODIS (pond fraction relative to ice area) available at the web page of University of Hamburg: http://icdc.zmaw.de/arctic_meltponds.html?&L=1 have been converted into pond fraction relative to pixel area using the provided ice concentration. Corresponding 8 day averages have been created from the MPD daily gridded data. The selection of valid grid cells in the dataset by Rösel et al., (2012) is the following: not less than 50% valid pixels for a valid grid cell, ice concentration greater than 25%, STD of MPF less than 15%. The comparison plot is shown in Figure 6. It is apparent that for the June 18, 2007 both datasets show similar spatial patterns with higher MPF between the Queen Elisabeth Islands and Beaufort Sea, and lower MPF in the MYI region north to Greenland and eastern part of the Arctic Ocean. This pond fraction distribution seems plausible when considering the date of observation, before melt onset in the MYI region, and such a spatial distribution is confirmed by both algorithms. The MPF values slightly differ in amplitude (note the distribution of higher and lower MPF in both datasets e.g. in the Beaufort Sea). The primary reason for this difference is likely the contrast in cloud screening methods between the two datasets, with MODIS much better suited to cloud screening over snow, resulting in differences in the fraction of unscreened clouds between both datatsets. The second reason is the different averaging method, with data by Rösel et al., (2012) being produced as a composite (best or most characteristic observation within the period), whereas MPD data is obtained by unweighted averaging. And finally the third reason for the difference is the positive 8% offset of the dataset by Rösel et al., (2012) as provided in the "Data quality" section at the data source http://icdc.zmaw.de/arctic_meltponds.html?&L=1. It is unclear whether

9

this bias is constant over the whole range of MPFs and if it is possible to correct for it. Mäkynen et al., (2014) suggest that the bias stems from possibly inaccurate assumption about sea ice optical properties, which would mean that the bias varies not only with MPF, but also with weather conditions and location in the Arctic ocean.

The second row of Figure 6 shows the same comparison, but for June, 18, 2011. Here again, both algorithms agree on the spatial distribution of the melt ponds, with slight differences in the amplitude, and thus confirm the plausibility of results presented both in Sect. 3.1 and in Rösel and Kaleschke, (2012).

3.3 Spatial trends of MPFs for the Arctic Ocean over the whole MERIS dataset (2002-2011)

As seen from the comparison to in situ data and reanalysis temperature data, the MPD retrieval is affected by unscreened high thin clouds, to which none of the available cloud filters are sensitive but which affect the retrieved MPF and albedo because clouds tend to increase the albedo/decrease pond fraction for areas of high true MPF and increase MPF/decrease albedo for areas of no or little melt. This produces an offset at the low MPFs and is mainly visible at the beginning of the melt season. It affects also the maximum reachable MPFs at the peak of the melt and the minimum MPFs before and after the season. The performance of the algorithm is compromised during the end of the melt season due to the presence of overfrozen, snow covered or melted through melt ponds.

Nevertheless, for the MERIS data the temporal dynamics of the retrieved quantities compares well with the NCEP surface air temperature data and the weekly averages show pronounced spatial variability of the retrieved pond fractions for different years which cannot be explained by thin cloud cover. This gives us the possibility to study the trends of the retrieved quantities as a potential systematic offset due to clouds would be cancelled out and only the variability of the true value shows up in the trend (Figure 7). The trend significance given by the map of the MPF trend p value (Figure 8) confirms this finding: the strongest positive or negative trends are the most significant ones with the p value of about 0.05-0.1. Given the small size of the studied sample (10 points), the statistically significant p value is expected to be greater than that of the larger samples. Therefore the p values obtained here can be used to select the

10

1 trend candidates. One more criterion that supports the statistical significance of the discovered

2 trends is the spatial continuity of the p value that suggests the non-random nature of the

3 effect.

4 There is no trend for the first week of June throughout the years (Figure 7), except for a slight

5 positive trend of MPF near Point Barrow. This feature disappears for the second week, and a

6 positive trend of 1-2 % during the early melt season is found near the Queen Elizabeth

7 Islands. This trend remains until the end of June. Explanation for this finding is not the

8 increase in the absolute value of the MPF, but rather the melt onset shifting towards spring in

9 these areas throughout the MERIS dataset (Figure 10). A negative trend in the East-Siberian

10 Sea has yet to be explained: either it is the opposite temporal shift of melt evolution towards

11 summer, or a shift of melt evolution towards spring with e.g. drainage phase of melt observed

12 instead of maximum melt, or a fluctuation in the weather conditions or in the ice type in the

13 area within the studied years. It is important to understand that the trend of the MPF can as

14 likely occur due to temporal shift of the melt process towards spring or autumn, as well as

15 change of maximum possible pond fraction due to ice type change. The maximum and

16 average MPFs depend not only on the air temperature, but also on the sea ice roughness on

17 various scales and other ice properties (Polashenski et al., 2012), so an increasing air

18 temperature trend in the area would not necessarily produce an increasing MPF trend. The

19 time sequence of MPF for the studied years for the location of interest in the East Siberian

20 Sea (74°N, 160°E averaged 50 km around the point) is shown in Figure 9.

21 The MPF curves for different years hardly show any temporal shift, but display a change of

22 absolute MPF and of temporal behavior of the melt evolution, which is an indication of an ice

23 type change from FYI to MYI. E.g. the curve corresponding to 2011 in Figure 9 (red curve)

24 shows a clear MYI MPF dynamics. The presence of MYI in the area is confirmed by

25 analyzing the maps of ice concentration for the autumn before in the region of interest (not

26 shown here, for details see AMSR-E ice concentration maps provided by Uni Bremen,

27 http://www.iup.uni-bremen.de:8084/databrowser.html). At the same time, a similar plot

28 (Figure 10) for the Queen Elizabeth Islands (50 km around 78°N, 108°W) displays the exact

29 opposite: the peak of MPF for the melt onset shifts towards spring in the later years of the

30 MERIS dataset, whereas the absolute value of the MPF peak stays the same. This is the sign

11

1 of warm air masses appearing earlier in the summer than before, producing the positive MPF

2 trend for the area.

3 The MPF trend for the 4th week of June features earlier melt onset in the MYI regions and

4 further melt overall in the Arctic ocean with occasional hints of longitudinal oscillations, e.g.

5 in week 4 of June, Figure 7.

6 3.4 Spatial trends of broadband sea ice albedo for the Arctic Ocean over the
7   whole MERIS dataset (2002-2011)

8 The MPF and the broadband albedo of the pixel are joint products, i.e. an increasing trend for

9 MPF gives a decreasing trend of the albedo. A decreasing albedo trend around the Queen

10 Elizabeth Islands and increasing trend in the East-Siberian Sea (see Figure 11) correspond

11 well to dynamics of the apparent MPF weekly trends (Figure 7) and are confirmed by low p-

12 values (Figure 12). The slight differences in spatial patterns of albedo and MPF trend can be

13 explained by different sensitivity of both retrievals to ice type and its optical properties: the

14 albedo retrieval translates the change of ice reflectance into the albedo of the pixel, whereas

15 the MPF retrieval only retrieves MPF. The albedo trend significance which displays similar

16 spatial pattern as the significance of the MPF trend (Figure 8) is shown in Figure 12. As can

17 be seen from the albedo trend significance, the remaining areas did not show clear albedo

18 trend within the studied period of time.

19 4 Conclusions

20 This publication presents a detailed analysis of the MPD product (Istomina et al., 2015; Zege

21 et al., 2015) consisting of a comparison to reanalysis air surface temperatures, detailed

22 analysis of weekly averages for 2007 and 2011 which showed different dynamics of MPF, but

23 resulted in similar minimum sea ice extent, comparison to the data by Rösel et al., (2012), and

24 analysis of albedo and MPF trends. The gridded products compare well to independent

25 reanalysis temperature data and show melt onset when the temperature gets above zero

26 degrees Celsius (Figure 2), however MPD results show an offset at low MPF of about 10%

27 most probably due to unscreened high clouds. This makes application of the MPD algorithm

28 to a sensor with a more precise cloud mask desirable (VIIRS onboard Suomi NPP or OLCI

29 onboard Sentinel3). Though absolute daily values of MPF and albedo may be affected by

12

1 unscreened clouds, relative MPF and albedo differences through the temporal axis are
2 significant and the temporal MPF dynamics correspond to that observed in the field for FYI
3 and MYI (Figure 2). This is also applicable to weekly averages based on analysis of MPF
4 behavior in 2007 and 2011 (Figure 3, Figure 4) and on the comparison of the MPD product to
5 data by Rösel et al., (2012) (Figure 6). Thus, the MPD products are suitable for analyzing
6 temporal and spatial dynamics of MPF and sea ice albedo.

7 Weekly averaged trends show pronounced dynamics of both MPF and albedo: a negative
8 MPF trend in the East Siberian Sea connected to a change of absolute MPF value in its peak
9 but no temporal shift, a positive MPF trend around the Queen Elizabeth Islands connected to
10 the earlier melt onset but with peak MPF values staying the same (Figure 7, Figure 9, Figure
11 10). The MPF dynamics in the East Siberian Sea could indicate a change of ice type
12 prevailing in the region, as opposed to the Queen Elizabeth Island, where the MPF dynamics
13 react to earlier onset of melt. This will be analyzed further in a follow-up publication.

23

13

1   **References**

2   Arndt, S. and Nicolaus, M.: Seasonal cycle and long-term trend of solar energy fluxes through
3   Arctic sea ice, Cryosph., 8(6), 2219–2233, doi:10.5194/tc-8-2219-2014, 2014.

4   Cavalieri, D. J. and Parkinson, C. L.: Arctic sea ice variability and trends, 1979–2010,
5   Cryosph., 6(4), 881–889, doi:10.5194/tc-6-881-2012, 2012.

6   Comiso, J. C.: Large Decadal Decline of the Arctic Multiyear Ice Cover, J. Clim., 25(4),
7   1176–1193, doi:10.1175/JCLI-D-11-00113.1, 2012.

8   Eicken, H., H. R. Krouse, D. Kadko, and D. K. Perovich: Tracer studies of pathways and rates
9   of meltwater transport through Arctic summer sea ice, J. Geophys. Res., 107(C10), 8046,
10 doi:10.1029/2000JC000583, 2002.

11 Istomina, L., Nicolaus, M. and Perovich, D.: Spectral albedo of sea ice and melt ponds
12 measured during POLARSTERN cruise ARK XXII/3 (IceArc) in 2012. PANGAEA Dataset.,
13 doi:10.1594/ PANGAEA.815111, 2013.

14 Istomina, L. G., Heygster, G., Schwarz, P., Birnbaum, G., Scharien, R. K., Polashenski, C.,
15 Perovich, D. K., Zege, E. P., Malinka, A. V., Prikhach, A. S. and Katsev, I. L.: The melt pond
16 fraction and spectral sea ice albedo retrieval from MERIS data I: validation against in situ,
17 aerial and ship cruise data, Cryosph., 2015.

18 Kalnay, E., Kanamitsu, M., Kistler, R., Collins, W., Deaven, D., Gandin, L., Iredell, M., Saha,
19 S., White, G., Woollen, J., Zhu, Y., Leetmaa, A., Reynolds, R., Chelliah, M., Ebisuzaki, W.,
20 Higgins, W., Janowiak, J., Mo, K. C., Ropelewski, C., Wang, J., Jenne, R. and Joseph, D.:
21 The NCEP/NCAR 40-Year Reanalysis Project, Bull. Am. Meteorol. Soc., 77(3), 437–471,
22 doi:10.1175/1520-0477(1996)077<0437:TNYRP>2.0.CO;2, 1996.

23 Mäkynen, M., Kern, S., Rösel, A. and Pedersen, L.: On the Estimation of Melt Pond Fraction
24 on the Arctic Sea Ice With ENVISAT WSM Images, Geoscience and Remote Sensing, IEEE
25 Transactions 52(11), 7366–7379, doi: 10.1109/TGRS.2014.2311476, 2014.

26 Perovich, D. K., Jones, K. F., Light, B., Eicken, H., Markus, T., Stroeve, J. and Lindsay, R.:
27 Solar partitioning in a changing Arctic sea-ice cover, Ann. Glaciol., 52(57), 192–196, 2011.

28 Perovich, D. K., Meier, W., Tschudi, M., Gerland, S. and Richter-Menge, J.: Sea ice, Arct.
29 Rep. Card 2012, http//www.arctic.noaa.gov/reportcard, 2012.

30 Polashenski, C., Perovich, D. and Courville, Z.: The mechanisms of sea ice melt pond
31 formation and evolution, J. Geophys. Res., 117(C1), C01001, doi:10.1029/2011JC007231,
32 2012.

14

1 Rösel, A. and Kaleschke, L.: Exceptional melt pond occurrence in the years 2007 and 2011 on
2 the Arctic sea ice revealed from MODIS satellite data, J. Geophys. Res., 117(C5), C05018,
3 doi:10.1029/2011JC007869, 2012.

4 Rösel, A., Kaleschke, L. and Birnbaum, G.: Melt ponds on Arctic sea ice determined from
5 MODIS satellite data using an artificial neural network, Cryosph., 6(2), 431–446,
6 doi:10.5194/tc-6-431-2012, 2012.

7 Schröder, D., Feltham, D. L., Flocco, D. and Tsamados, M.: September Arctic sea-ice
8 minimum predicted by spring melt-pond fraction, , 4(May), 353–357,
9 doi:10.1038/NCLIMATE2203, 2014.

10 Serreze, M. C. and Barry, R. G.: The Arctic Climate System, Cambridge: Cambridge
11 University Press., 2005.

12 Shindell, D. and Faluvegi, G.: Climate response to regional radiative forcing during the
13 twentieth century, Nat. Geosci., 2(4), 294–300, doi:10.1038/ngeo473, 2009.

14 Stroeve, J. C., Serreze, M. C., Holland, M. M., Kay, J. E., Malanik, J. and Barrett, A. P.: The
15 Arctic's rapidly shrinking sea ice cover: a research synthesis, Clim. Change, 110(3-4), 1005–
16 1027, doi:10.1007/s10584-011-0101-1, 2011.

17 Wang, C., Granskog, M., Gerland, S., Hudson, S. R., Perovich, D. K., Nicolaus, M., Ivan
18 Karlsen, T., Fossan, K. and Bratrein, M.: Autonomous observations of solar energy
19 partitioning in first-year sea ice in the Arctic Basin, J. Geophys. Res. C Ocean., 119, 2066 –
20 2080, doi:10.1002/2013JC009459, 2014.

21 Zege, E. P., Malinka, A. V., Katsev, I. L., Prikhach, A. S., Heygster, G., Istomina, L. G.,
22 Birnbaum, G. and Schwarz, P.: Algorithm to retrieve the melt pond fraction and the spectral
23 albedo of Arctic summer ice from satellite data, Remote Sens. Environ., 163, 153-164,
24 doi:10.1016/j.rse.2015.03.012, 2015.

25

26

15
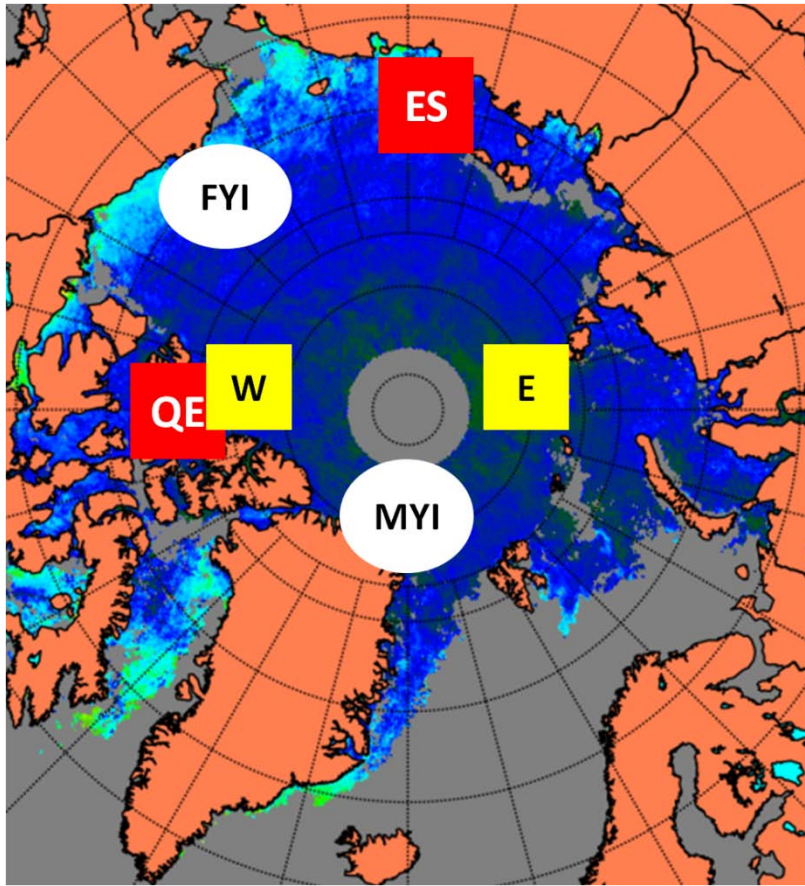
1

2

3　Figure 1. The scheme of the case study locations (the size of the labels does not correspond to

4　the real size of the studied area, see text for area sizes). White circles depict locations for the

5　time sequence analysis in summer 2009, in the Beaufort Sea, FYI (red curves in Figure 2) and

6　North Greenland, MYI (blue curves in Figure 2). Yellow squares show locations for two sites

7　in both 2007 and 2011, namely in Barents Sea (E) and north to the Queen Elizabeth Islands

8　(W) (Figure 5). Red squares depict the locations of two sites between Queen Elizabeth Islands

9　(Figure 10) and in the East Siberian Sea (Figure 9), where the MPF temporal behavior was

10　compared for years 2002-2011.

11
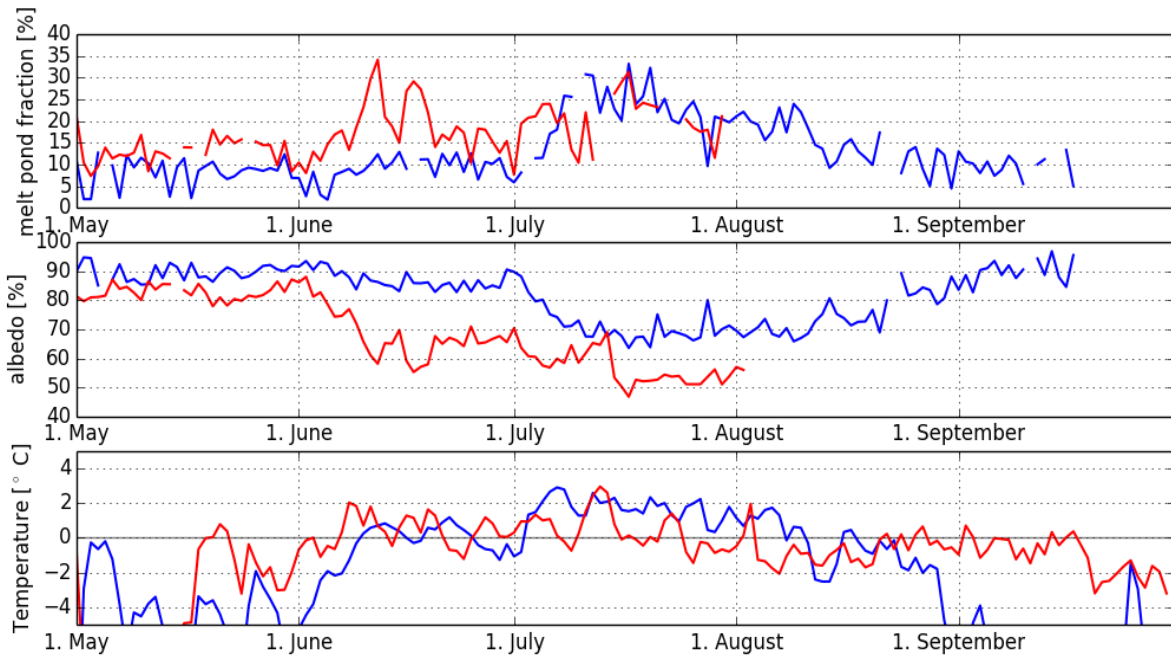
1

2   Figure 2. Time sequence of MPF, broadband albedo and NCEP air temperature at the surface

3   for two regions: FYI area in Beaufort Sea near Barrow (75°N, 155°W, shown in red) and MYI

4   area around North Greenland (84.5°N, 35°W, shown in blue) May to September 2009.

5   Locations are shown in Figure 1 with white circles tagged "FYI" and "MYI", respectively.

6   The albedo and MPF curves in the FYI area are interrupted as the area becomes completely

7   ice free on the 1st of August 2009.

17
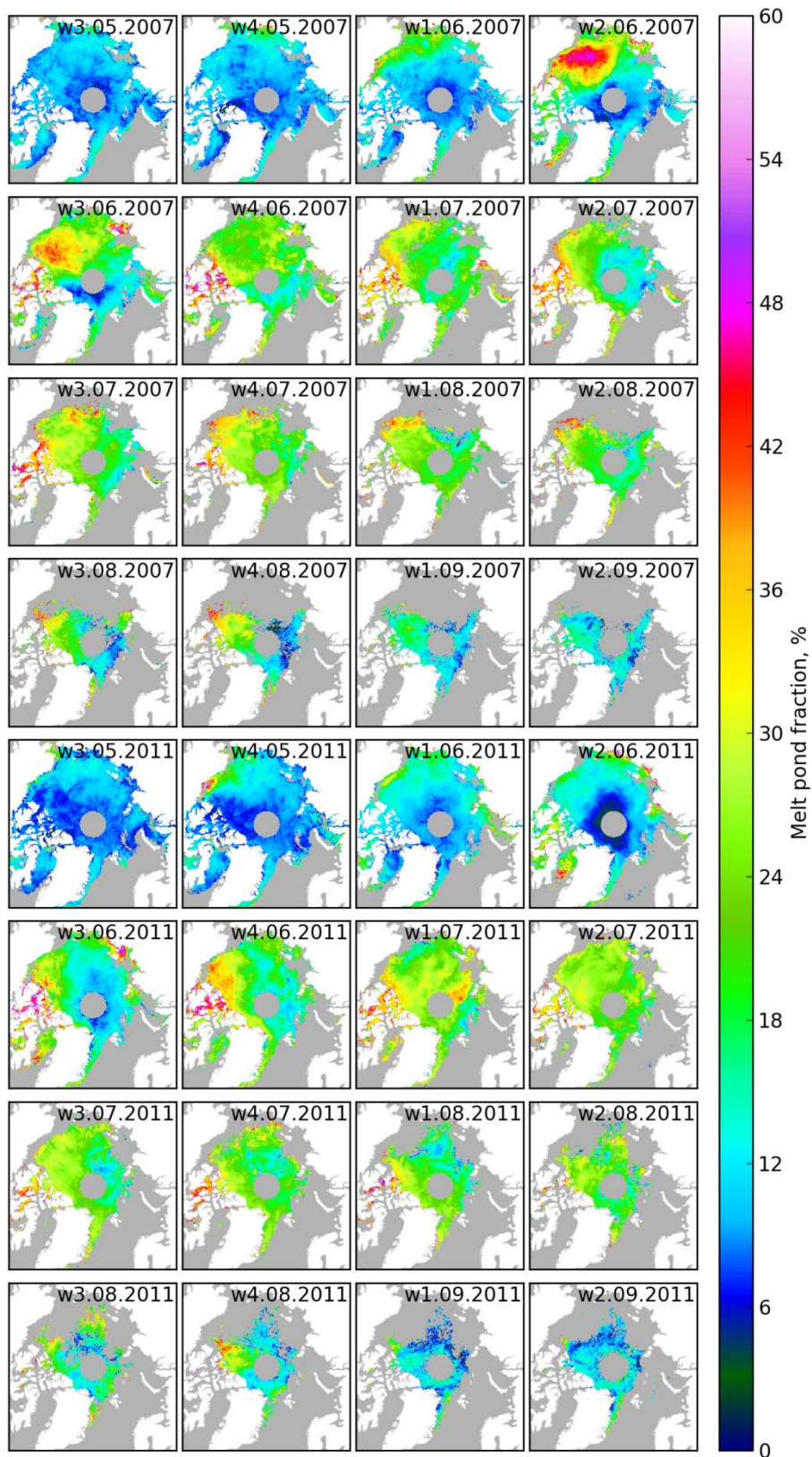
Figure 3. Retrieved weekly averaged MPF for summer 2007 and 2011.

18
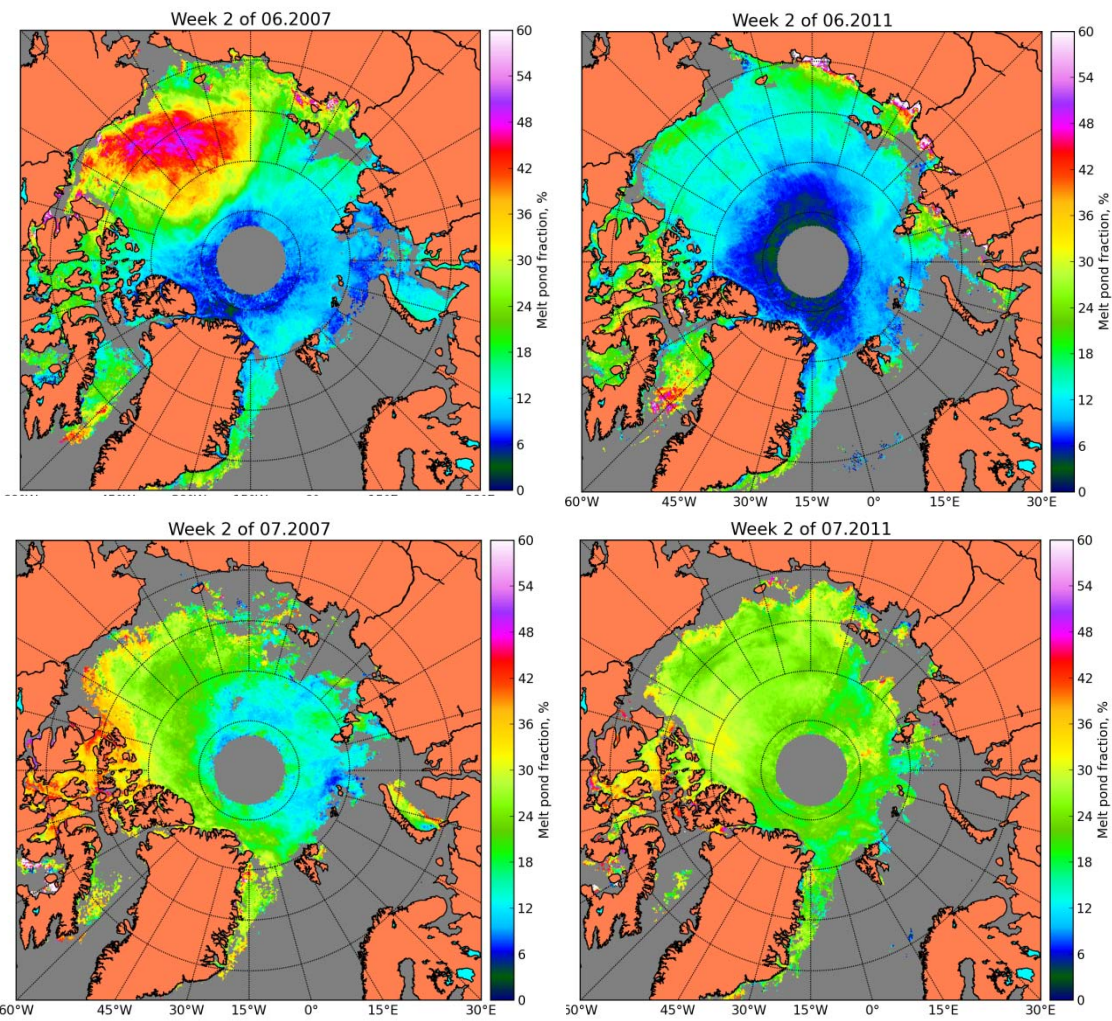
1

2

3   Figure 4. Main differences of weekly MPF averages 2007 and 2011 (Figure 3). Comparison

4   of the weekly average pond fraction for the second week of June 2007 and 2011 (top row, left

5   and right correspondingly) and for the second week of July 2007 and 2011 (bottom row, left

6   and right correspondingly). Note the drastic melt onset in the 2nd week of June 2007, but

7   lower MPFs in the 2nd week of July 2007 compared to 2011.

8
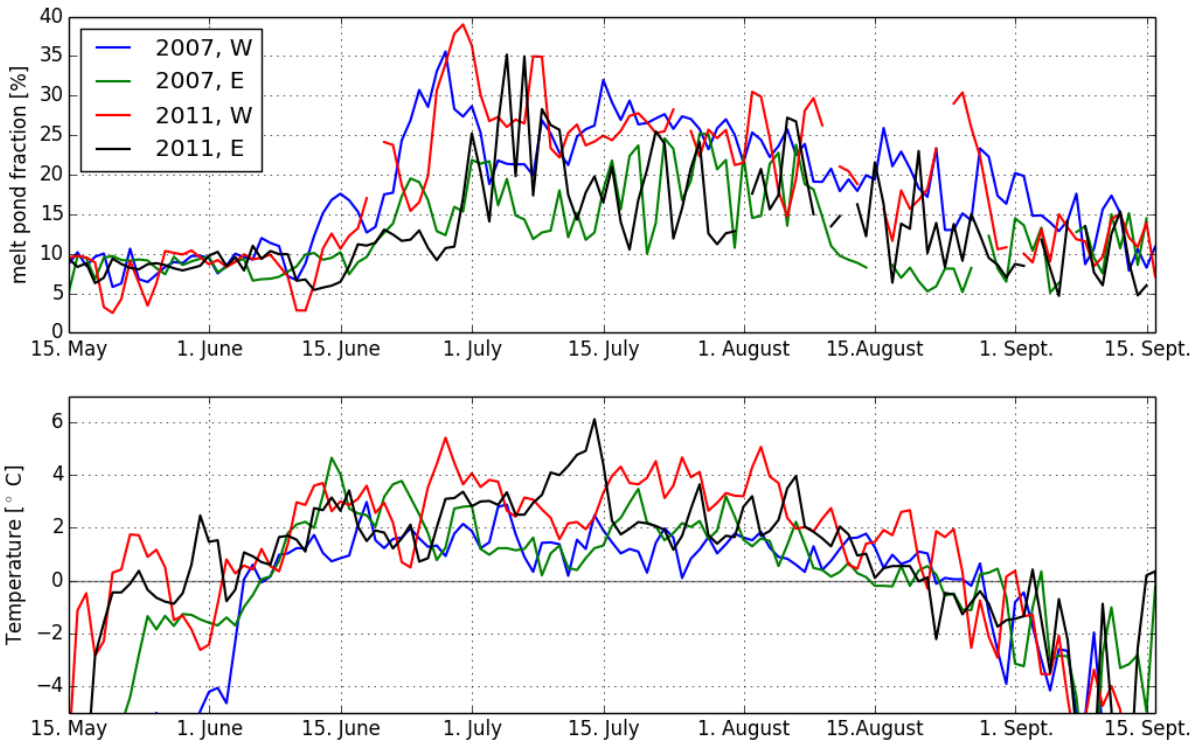
19

Figure 5. Daily averages of MPF (top panel) and NCEP air temperature at the surface (bottom panel) for two locations with the similar melt dynamics ("reference") and diverse melt dynamics ("characteristic"): reference location to the north to the Queen Elizabeth Islands, 83°N, 110°W (tag "W" in the legend), 2007 (blue curves) and 2011 (red curves) and characteristic location in the Barents Sea, 85°N, 65°E (tag "E" in the legend), 2007 (green curves) and 2011 (black curves). Locations are shown in Figure 1.
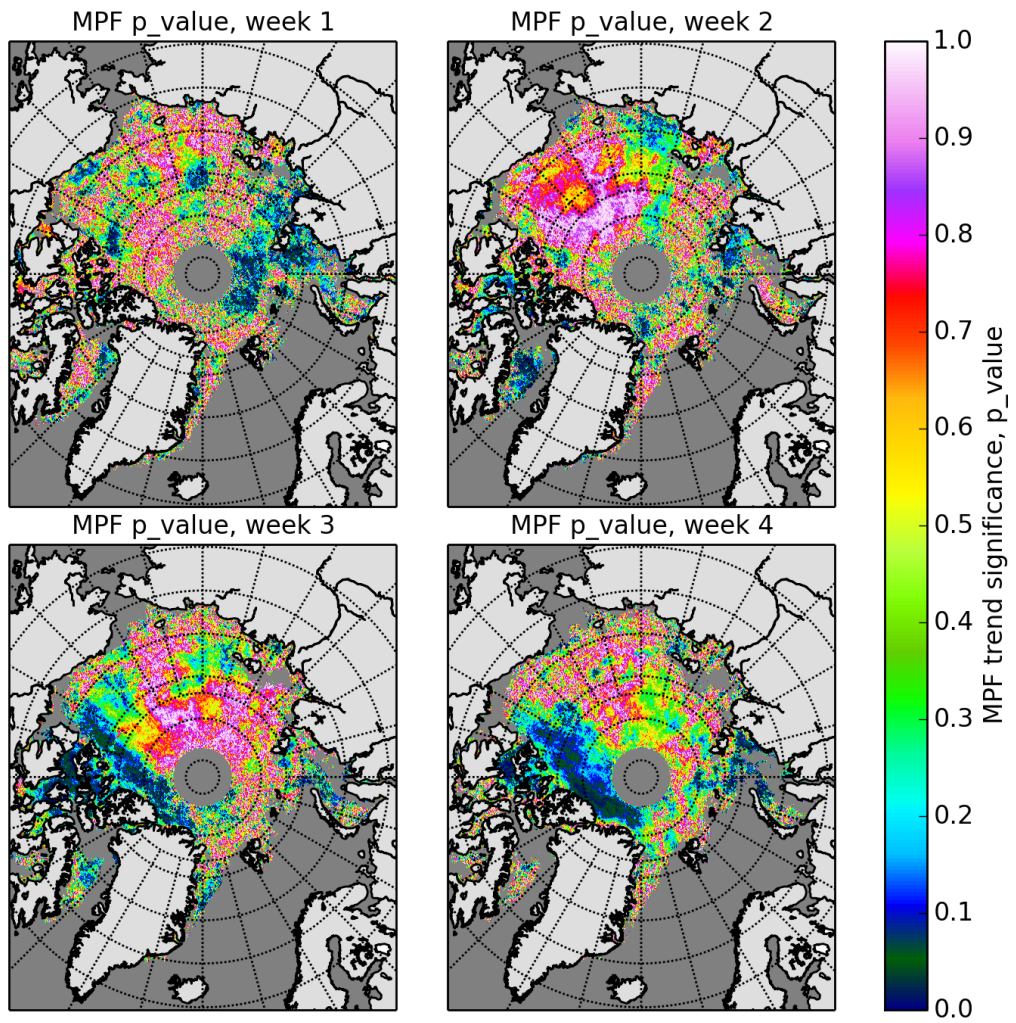
20
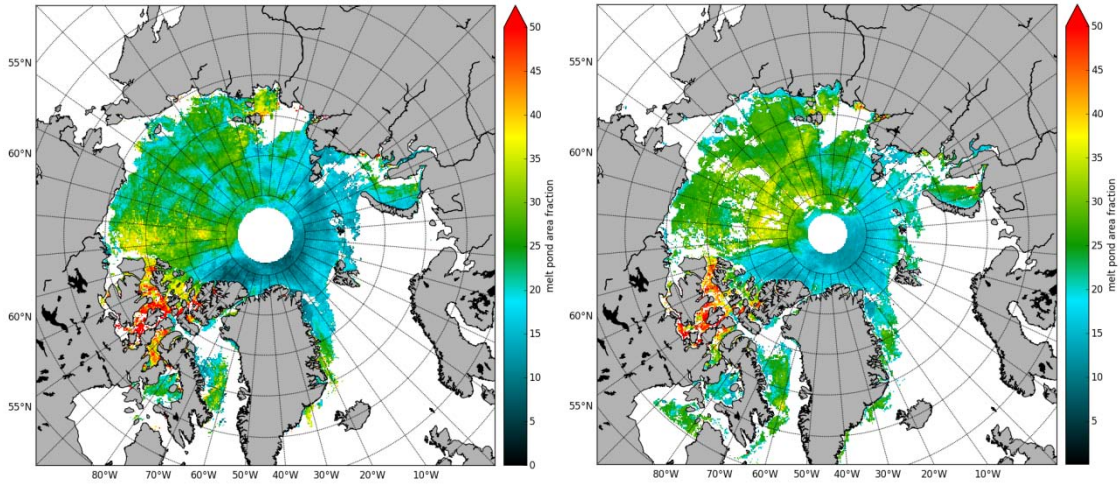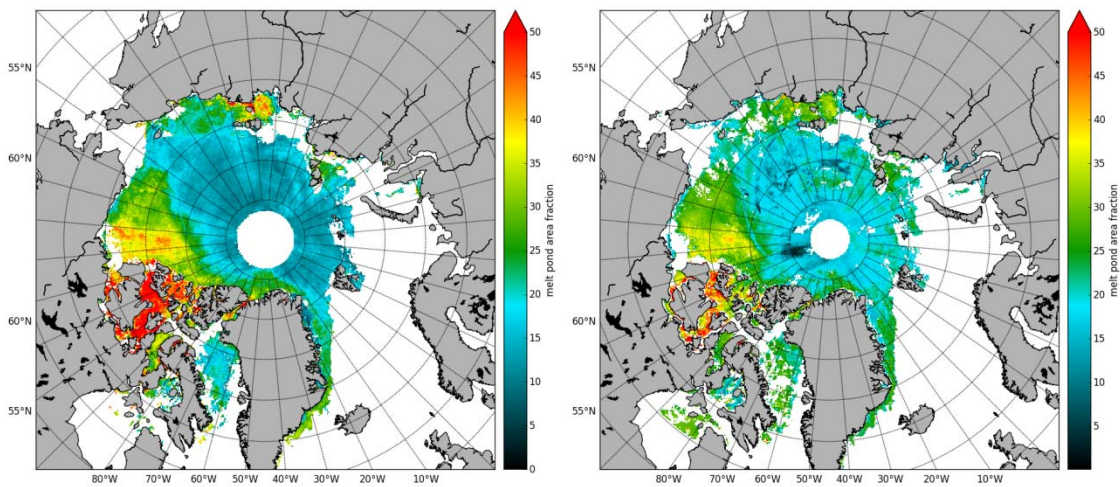
Figure 6. Comparison of the MPD MPF (8 day average, left column) to the MPF from (Rösel and Kaleschke, 2012) (8 day composite, right column) for June 18, 2007 (top row) and June 18, 2011 (bottom row).
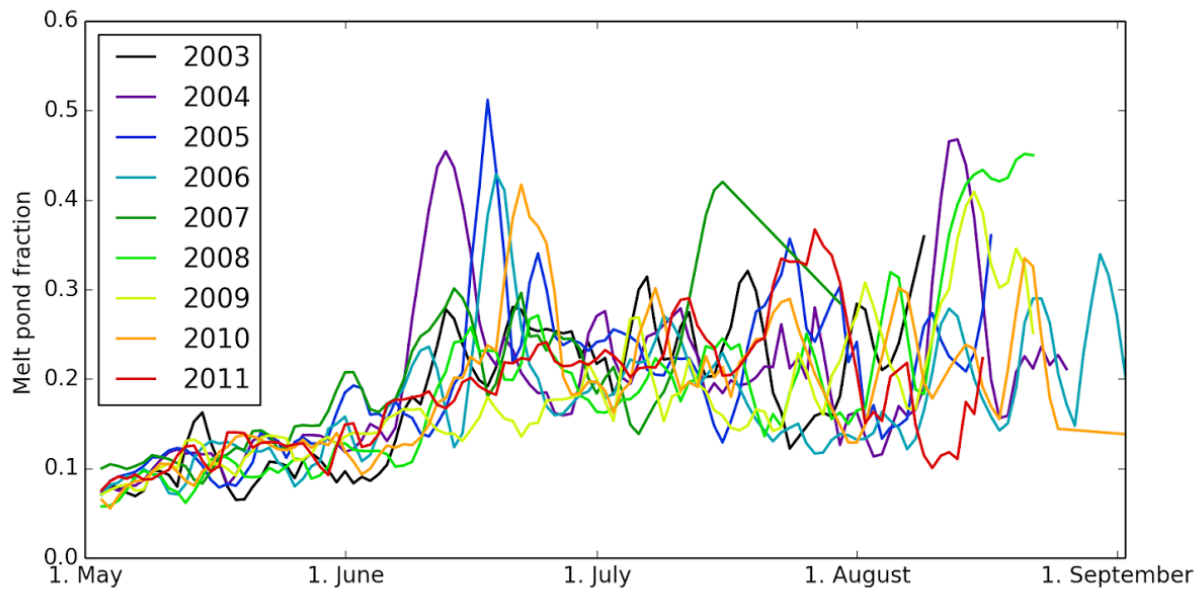
21
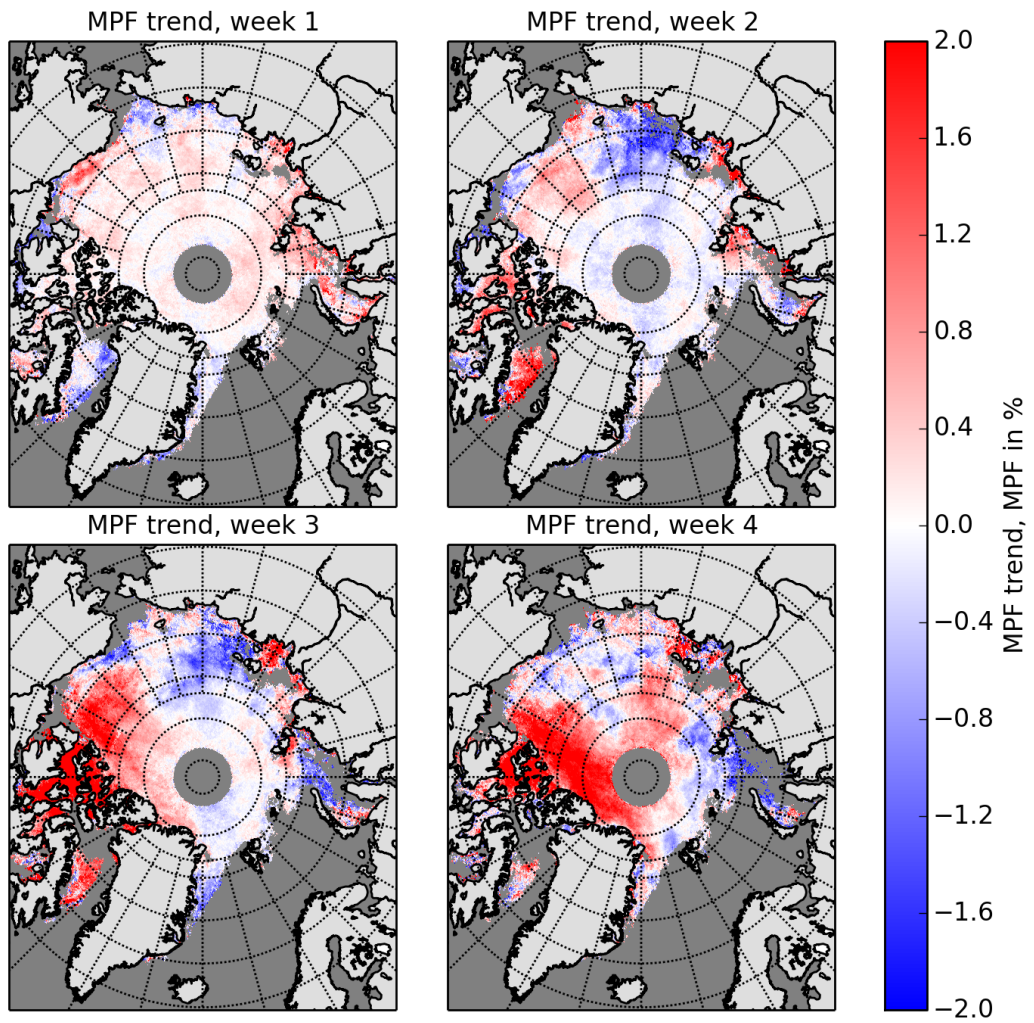
1

2 Figure 7. Melt pond fraction trends (trend in MPF %) for the four weeks of June for the whole

3 investigation period 2002-2011.

4

MPF p_value, week 1

MPF p_value, week 2

MPF p_value, week 3

MPF p_value, week 4

MPF trend significance, p_value

1

Figure 8. P values for the weekly MPF trends (see Figure 7).

3
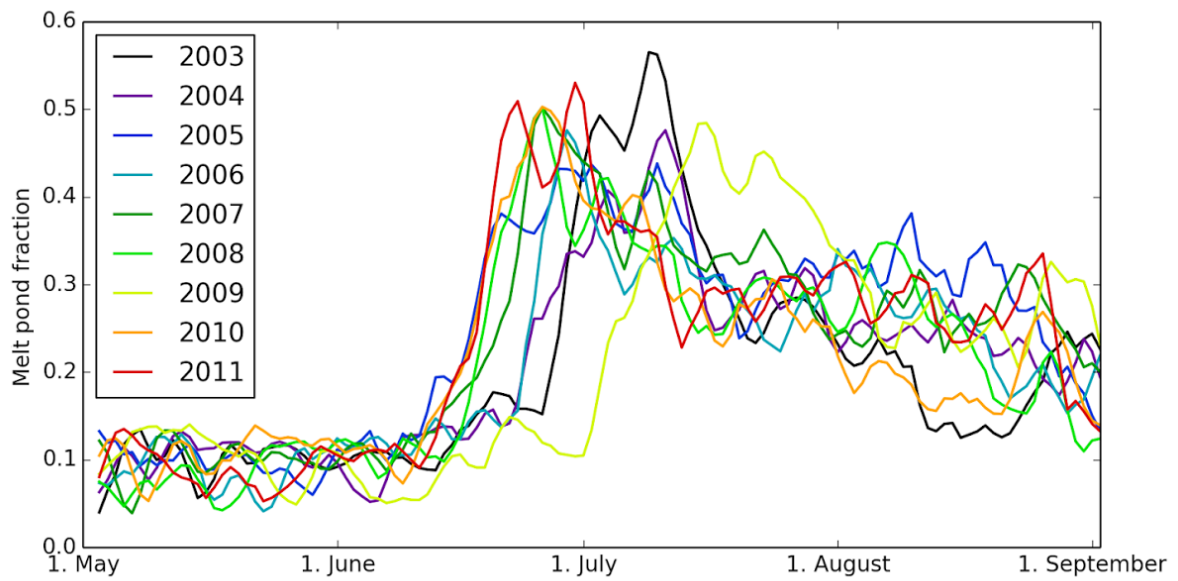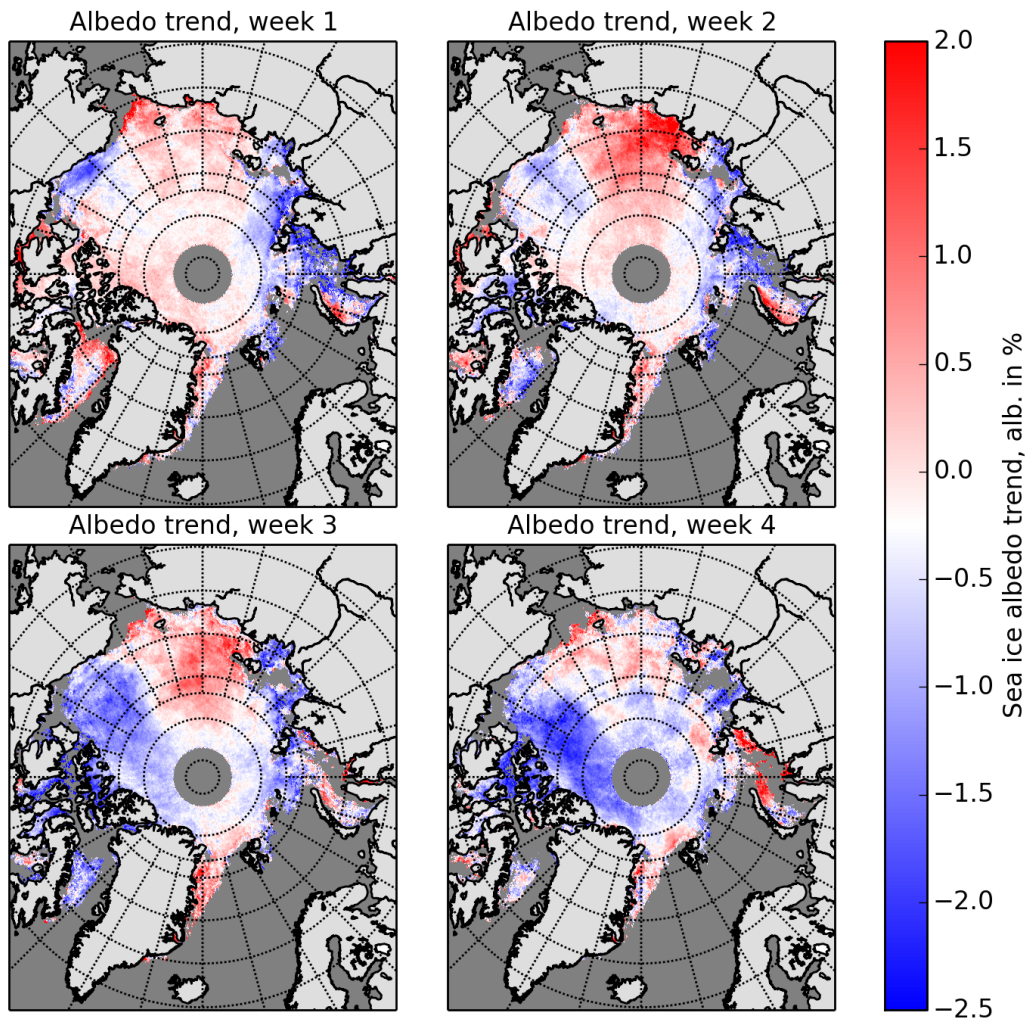
4

5

23

Figure 9. Time sequence of MPF for the studied years for the area of negative MPF trend in the East Siberian Sea (74°N, 160°E, marked with the red square "ES" in Figure 1). In the 2nd – 3rd week of June the MPF in the earlier years of the MERIS dataset reached high (up to 0.5) peak values as the melt onset started, which is typical for the first year ice. In the later years, however, the behavior of the MPF more resembles that on the MYI: no rapid melt onset, lower peak values of MPF. Running mean with window size 3 has been applied to the data.

24

1

2

3   Figure 10. Time sequence of MPF for the studied years for the area of positive MPF trend in

4   the Queen Elizabeth Islands (78°N, 108°E, marked with the red square "QE" in Figure 1). In

5   the 3rd – 4th week of June the MPF in the earlier years of the MERIS dataset reached peak

6   values later in the summer as compared to later years, and melt onset in the later year happens

7   earlier than before. Running mean with window size 3 has been applied to the data.

8

25

Albedo trend, week 1

Albedo trend, week 2

Albedo trend, week 3

Albedo trend, week 4

Sea ice albedo trend, alb. in %

1

2

3   Figure 11. Broadband sea ice albedo trends (trend in albedo %) for the four weeks of June for

4   the whole investigation period 2002-2011.

5

26
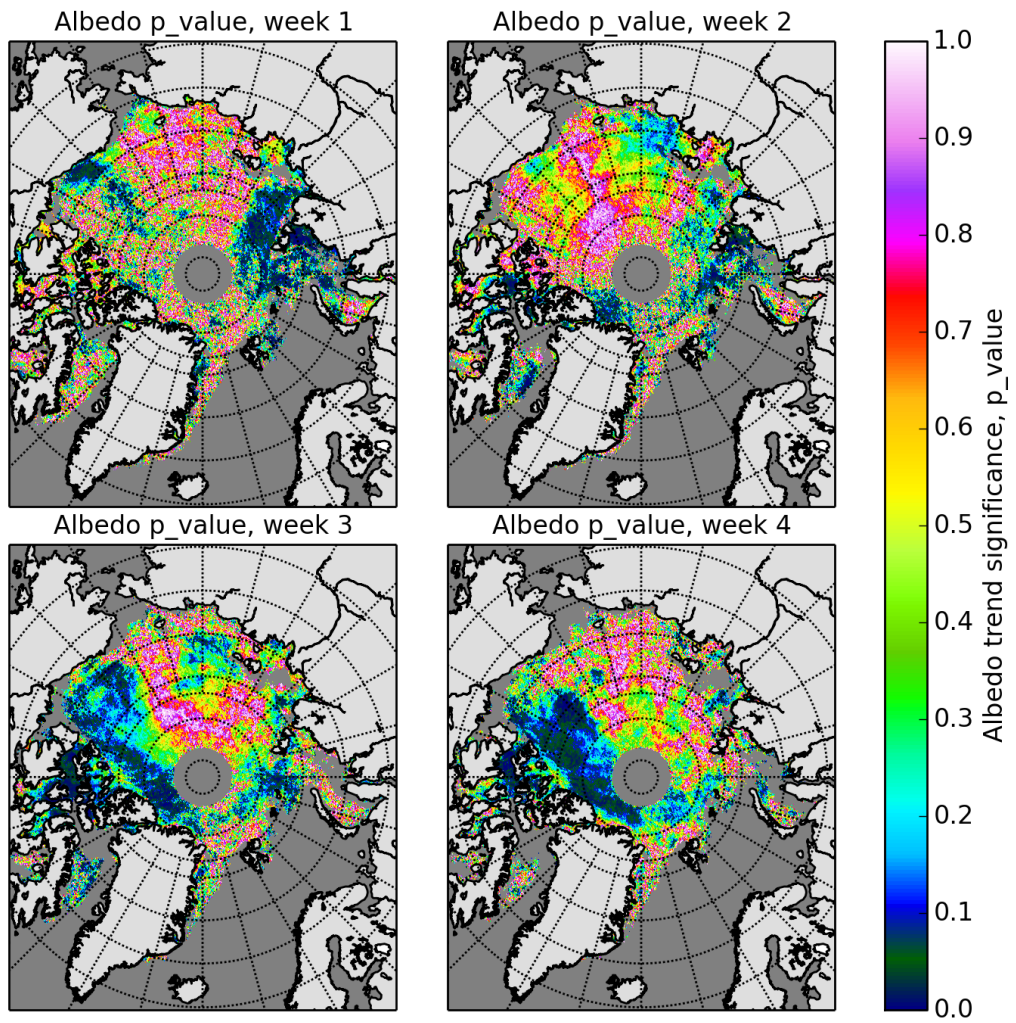
Figure 12. P values for the weekly broadband albedo trends (see Figure 11).

27